# Spatio-temporal coordination at the maternal-fetal interface promotes trophoblast invasion and vascular remodeling in the first half of human pregnancy

Shirley Greenbaum[1,2,*,+], Inna Averbukh[1,+], Erin Soon[1,3,+], Gabrielle Rizzuto[4], Alex Baranski[1], Noah Greenwald[1,5], Marc Bosse[1], Eleni G. Jaswa[6], Zumana Khair[1], Shirley Kwok[1], Shiri Warshawsky[1], Geneva Miller[7], Morgan Schwartz[7], Will Graf[7], David Van Valen[7], Leeat Keren[8], Travis Hollmann[9], Matt van de Rijn[1], Michael Angelo[1, *]

[+]Equal contribution

[*]Correspondence: greenbaumsh@gmail.com (S.G.), mangelo0@stanford.edu (M.A.)

[1]Department of Pathology, Stanford University

[2]Department of Obstetrics & Gynecology, Hadassah-Hebrew University Medical Center

[3]Immunology Program, Stanford University

[4]Department of Pathology, UCSF

[5]Cancer Biology Program, Stanford University

[6]Department of Obstetrics, Gynecology & Reproductive Sciences, UCSF

[7]Division of Biology and Bioengineering, California Institute of Technology

[8]Department of Molecular Cell Biology, Weizmann Institute of Science

[9]Department of Pathology, Memorial Sloan Kettering Cancer Center

# Abstract

Beginning in the first trimester, fetally derived extravillous trophoblasts (EVTs) invade the uterus and remodel its spiral arteries, transforming them into large, dilated blood vessels that lack smooth muscle and are partially lined with EVTs instead of vascular endothelium. Several mechanisms have been proposed to explain how EVTs coordinate with decidual cells to promote a tissue microenvironment conducive to spiral artery remodeling (SAR). However, it remains a matter of debate which immune and stromal cell types participate in these interactions, how this process evolves with respect to gestational age, and which anatomic routes are the predominate path of EVT invasion in humans. To elucidate this complex interplay, we used multiplexed ion beam imaging by time of flight with a 37-plex antibody panel to build the first spatio-temporal atlas of the human maternal-fetal interface in the first half of pregnancy at single-cell resolution. We analyzed ~500,000 cells and 588 spiral arteries within intact decidua from 66 patients between 6-20 weeks of gestation. Using custom machine learning algorithms for cell segmentation and classification, we evaluated the spatial distributions and phenotype of 20 maternal and five EVT populations with respect to gestational age and SAR. Gestational age substantially influenced the frequency of most maternal immune and stromal cells, with tolerogenic subsets expressing CD206, CD163, TIM-3, Galectin-9, and IDO-1 preferentially enriched at later time points. In contrast, SAR progression, and not gestational age, preferentially correlated with local invasion of EVTs. Lastly, by comparing spatial co-occurrence and phenotype of decidual interstitial, perivascular and intravascular EVTs with respect to SAR progression, we developed a statistical model suggesting an intravasation mechanism as the predominant route of EVT invasion in superficial decidua. Taken together, these results support a coordinated model of decidualization in which increasing gestational age drives a transition in maternal decidua towards a tolerogenic niche conducive to locally regulated, EVT-dependent SAR.


# Introduction

The maternal-fetal interface is established when the trophoectoderm cells of the blastocyst invade the decidualizing endometrial stroma, ultimately forming the placenta. From that point forward, normal development depends on a complex interplay between maternal cells and placental trophoblasts that ultimately transforms the nascent womb into a specialized niche capable of meeting the metabolic demands of a growing hemi-allogeneic fetus while maintaining maternal tolerance[1–5]. Rather than being a single monotonic trend, this process is multifaceted and dynamic with respect to both tissue structure and gestational age (GA). Subsequent to implantation, decidual cellular composition shifts to one that is enriched for invasive extravillous trophoblasts (EVTs)[6]. During this transition, maternal and fetal cells remodel uterine spiral arteries into highly dilated vessels with minimal smooth muscle where EVTs have partially replaced the

maternal endothelium within the arterial lumen[7–9]. Spiral artery remodeling (SAR) in healthy pregnancies results in low-resistance vessels that can deliver blood to the intervillous space at low flow velocities that prevent damage to the placental architecture[10,11]. Conversely, impaired SAR, fewer tolerogenic maternal cells, and abnormal decidual invasion of EVTs have each been implicated in placenta-related obstetric complications, including preeclampsia, intrauterine growth restriction, and preterm birth[12,13]. Therefore, detailed investigation of the cell population dynamics at the maternal-fetal interface is key to understanding the biology of normal pregnancy and the pathophysiology of placenta-related obstetric complications.

Due to the poor feasibility of controlled studies in pregnant humans, much of what is known about maternal-fetal tolerance and SAR is based on pregnancy in small mammals[14]. Although some similarities exist, key facets of hemochorial placentation in humans are primate-specific, and in some cases are restricted even further to great apes[15–17]. For example, EVTs in mice only invade the superficial decidua, do not replace the vascular endothelium, and are thought to play a minor role in SAR compared to maternal uterine natural killer (NK) cells[18]. In contrast, EVTs in humans invade completely through the decidua into the inner third of the myometrium and are considered to be vital for adequate SAR[3,19,20]. Since the most extensive EVT invasion has been observed in humans, it may be a key adaptation that permitted upright, bipedal locomotion while maintaining adequate blood flow in the third trimester when development of the large fetal brain accounts for 60% of metabolic needs [21,22].

The study of human decidual remodeling is further complicated by additional inherent challenges. First, cell composition and structure are temporally dynamic; aggregating data across different GAs or observing a single time point may be misleading. As endometrial stromal cells shift towards a decidualized phenotype[23,24], the functions of maternal NK cells, T cells, and macrophages change dynamically in the first and second trimesters to promote a permissive niche conducive to villus attachment and invasion. This process necessarily establishes a gradient of EVT invasion that advances inward from the superficial decidua. Consequently, decidual structure and composition in focal regions can differ significantly from its bulk attributes. A second major challenge arises in understanding how these global dynamics are coupled to processes requiring spatial

coordination, such as those between maternal and placental cells in the local tissue microenvironment. For example, periarterial decidual NK cells are thought to contribute to SAR both by initiating smooth muscle breakdown and by secreting chemokines that attract invading EVTs, while phagocytic macrophages are thought to facilitate clearance of the resultant apoptotic debris[25–27]. Overall, formation of the human maternal-fetal interface involves sophisticated spatiotemporal coordination such that tissue composition, structure, and function are inextricably coupled. Unraveling this interdependence requires an approach that can ascertain how these facets change over time in intact human tissue.

With this in mind, we constructed the first high dimensional spatio-temporal atlas of the human maternal-fetal interface. We leveraged archival tissue banks to assemble a cohort of maternal decidua from 66 women who underwent elective terminations of otherwise healthy pregnancies at 6-20 weeks gestation. We then performed high dimensional, subcellular imaging with multiplexed ion beam imaging by time of flight (MIBI-TOF) [28] using a 37-plex antibody panel designed to comprehensively identify the location, lineage, and function of all major maternal and placental cells. To understand how SAR relates to local decidual composition, we developed new algorithms for quantifying vascular morphology that enabled us to assign a remodeling score to each individual artery. Comparison of these scores for 588 arteries revealed that the extent of SAR to varies significantly with respect to GA. We then leveraged these discordances to discern which changes in decidual composition and structure were preferentially driven by GA, SAR, or both. Overall, the frequencies and relative proportions of maternal immune cells exhibited a robust temporal dependence that permitted us to predict GA based on these features alone. In contrast, we found that EVT invasion and perivascular localization were the dominant drivers of SAR in the tissue microenvironment. Given these findings, we then used our atlas to compare two models for the path of EVT migration from the cytotrophoblast cell columns to maternal spiral arteries that have been proposed previously: (1) intravasation, where EVTs first invade the decidua and then enter arteries by traversing the arterial wall, and (2) extravasation, where EVTs enter arteries directly at the basal plate[9]. Using statistical analyses correlating EVT phenotype and location with the extent of arterial smooth muscle and endothelial loss, we found that our spatiotemporal atlas was most consistent with an intravasation model. Taken

123 together, these investigations support a cooperative interplay in the first half of pregnancy
124 in which temporally dependent changes in decidual function permit placental EVTs to
125 extensively alter the maternal uterine vasculature.

126 # Results

127 ## Multiplexed imaging of human decidua reveals the tolerogenic composition of the
128 maternal-fetal interface

129 As part of the Human BioMolecular Atlas Program (HuBMAP) initiative, we created
130 the first spatio-temporal tissue atlas of the human maternal-fetal interface in the first 20
131 weeks of pregnancy (Fig. 1a). The goal of this study was to comprehensively define the
132 structure and composition of decidua and to understand how it changes during the first
133 two trimesters with respect to two axes: GA and maternal SAR. To examine these issues,
134 we assembled a retrospective cohort of archival formalin-fixed, paraffin-embedded
135 placenta and decidua tissue from 74 patients who underwent elective termination of
136 pregnancies with no known fetal abnormalities. Archival tissue blocks were manually
137 screened by a perinatal pathologist in hematoxylin and eosin (H&E) stained tissue
138 sections to determine which samples contained decidua. Then, regions of decidua that
139 contained spiral arteries were demarcated, cored, and assembled into two tissue
140 microarrays (TMAs) of 1mm and 1.5 mm cores. The final dataset included samples for 6-
141 20 weeks of gestation (13.72±4.8 weeks) from 66 patients of varying parity (1.45±1.72),
142 age (28.17±5.9 years), body mass index (28.19±7.3 kg/m$^2$), and ethnicity (Fig. 1b-f,
143 Supplementary Table 1). Due to inherent limitations in how the tissue was procured,
144 precise anatomic locations could not be determined. However, 61 out 66 tissue blocks
145 contained placental villi, suggesting that the vast majority of this cohort was sampled from
146 decidua basalis (Supplementary Table 2, See methods).

147 Previous studies of intact tissue examining only one or a few cell populations at a
148 time reported shifts in maternal immune cells towards tolerogenic states that are
149 permissive to invasion by fetally derived EVTs[19]. To gain a more complete picture of the
150 complex cell-cell interactions that establish maternal tolerance in the first half of
151 pregnancy, we designed and validated a 37-plex antibody panel for simultaneously

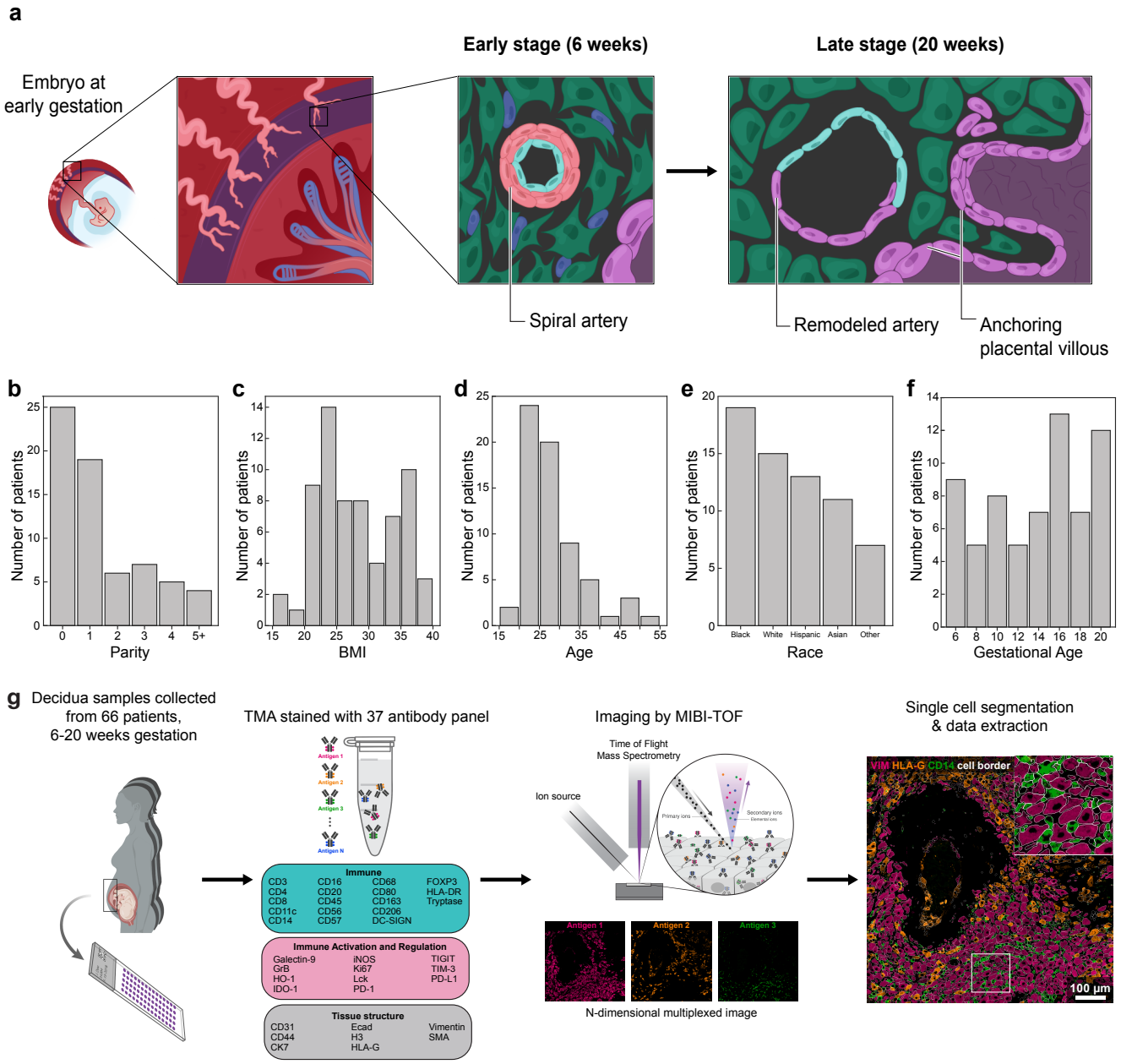


**Figure 1 | Study design and workflow. a.** Diagram of a human embryo in utero at 6 weeks gestation. First inset: the maternal-fetal interface consisting of decidua basalis (purple) with maternal spiral arteries (light pink) and fetal chorionic villi in the intervillous space (bottom right corner). Second inset: early stage (6 weeks) unremodeled spiral artery and progression to late stage (20 weeks) remodeled artery and anchoring fetal villi. **b.** Cohort parity distribution. **c.** Cohort distribution of body mass index (BMI). **d.** Cohort age distribution. **e.** Cohort ethnicity distribution. **f.** Cohort distribution of gestational age (GA). **g.** TMA construction, antibody panel, MIBI workflow, and single-cell segmentation.

152 mapping the functional state and location of all major maternal and fetal cell populations

153 (Fig. 1g, See methods, Extended Data Fig. S1). In addition to canonical lineage defining

markers for fetal cells, maternal immune cells, fibroblasts, smooth muscle, endothelium, and epithelium, we also quantified 10 functional markers previously implicated in maternal immune tolerance, including TIM-3, Galectin-9, PD-1, PDL-1, and IDO-1 (Fig. 1g, Extended Data Fig. S1)[29–34] . TMA sections were stained simultaneously with this antibody panel and subsequently imaged at 500 nm resolution using MIBI-TOF (Fig. 1g).

Multiplexed images were denoised with a low-level image analysis pipeline as described previously (Fig. 1g)[35]. To accurately capture the unique diversity of morphologically distinct maternal and fetal cells, we used our previously validated custom whole cell convolutional neural network, Mesmer[36] (See methods, Extended Data Fig. S2a). We optimized this neural network for decidua-specific segmentation by training with 93,000 manually annotated single cell events from 25 decidual images, 15 of them from our cohort. Applying this segmentation algorithm to our cohort images yielded 495,349 segmented cells in total, identified across 211 images (800μmx800μm, 2347±783 cells per image). FlowSOM clustering[37] was used to assign 92% of whole cell segmented events to 25 cell populations (Fig. 2a, b, See methods, Extended Data Fig. S2b, c, Supplementary Table 3). These data (Fig. 2c-g) were then combined with whole-cell segmentation masks to generate cell phenotype maps (CPM) in which each cell is colored categorically by its respective population (Fig. 2h, Extended Data Fig. S2d). We then determined whether cells expressed the functional markers by applying statistically derived per-marker binary expression thresholds (see Methods, Extended Data Fig. S2e, Supplementary Table 4). Noteworthy histological features—such as arteries, vessels, glands, the cell columns, and decidual tissue boundaries were manually annotated in collaboration with a perinatal pathologist.

Non-immune maternal (structural) cells accounted for the majority (56.3%) of all segmented events in the decidua and were predominantly composed of decidual fibroblasts (60.5%) and myofibroblasts (24.8%) with smaller contributions from vascular endothelium (7.6%) and glandular epithelial cells (7.1%, Fig. 2b, c). Maternal immune cells (31% of all cells) were dominated by macrophages (47.6% of immune) and NK cells (42.6% of immune) with minor contributions from T (8% of immune), dendritic (1.3% of immune), and mast cells (0.5% of immune). We identified a total of five decidual

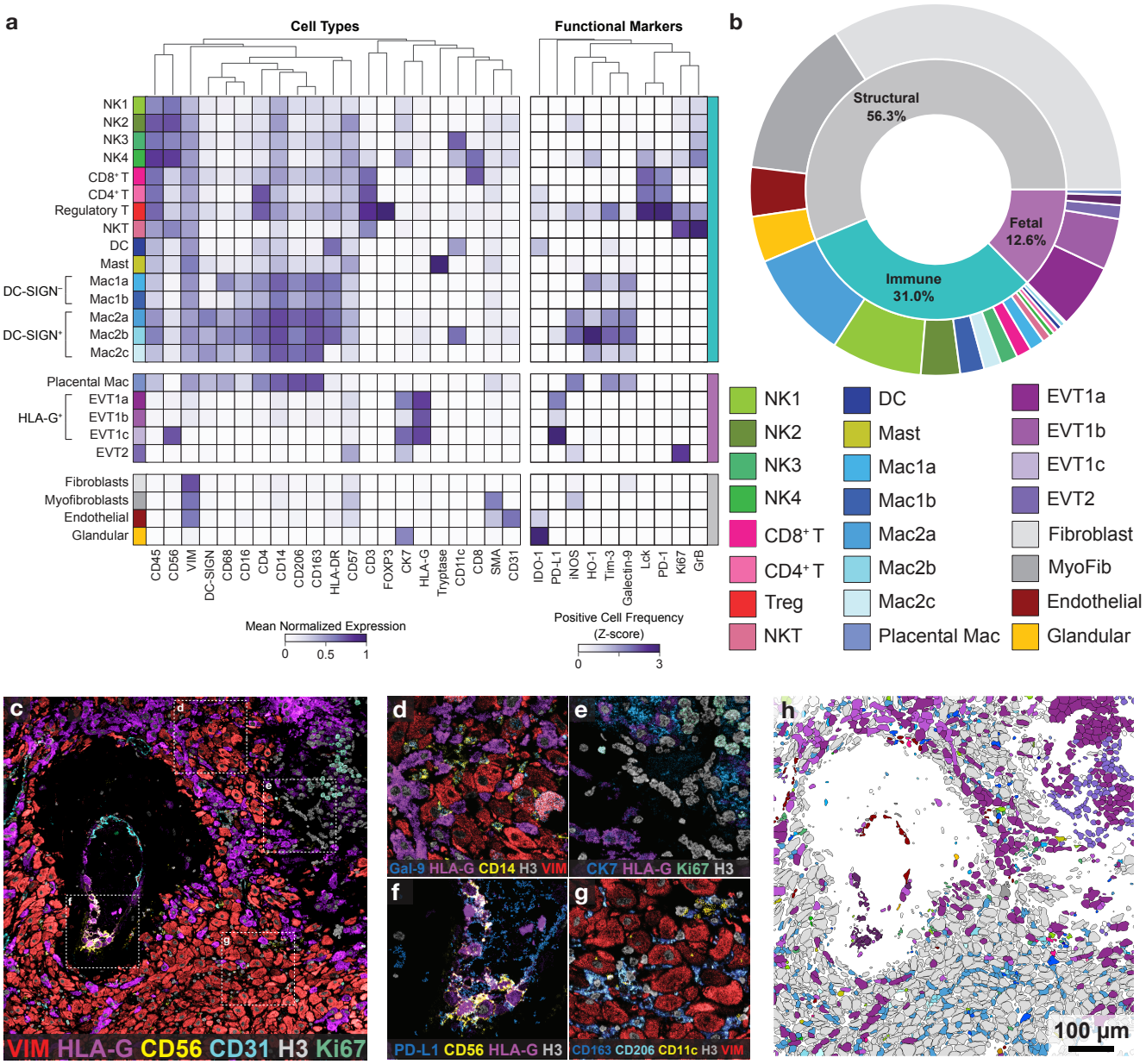


**Figure 2 | Multiplexed imaging of human decidua reveals the immune tolerance-conducive composition of the maternal fetal interface. a.** Cell lineage assignments showing mean normalized expression of lineage markers (left) and functional marker positive cell frequency (right, Z-score). Columns (markers) are hierarchically clustered. **b.** Cell lineage abundances across our cohort. Placental mac: Placental macrophage; MyoFib: Myofibroblast. **c.** Representative MIBI field of view color overlay of a 20 week sample. Red = VIM, vimentin, purple = HLA-G, yellow = CD56, cyan = CD31, grey = H3, green = Ki67. **d.** Inset of **c**, interstitial fetal EVTs. Blue = Galectin-9, purple = HLA-G, yellow = CD14, grey = H3, red = VIM **e.** Inset of **c**, showing anchoring villous cell column to decidua interface. Blue = CK7, cytokeratin7, purple = HLA-G, green = Ki67, grey = H3. **f.** Inset of **c**, showing intravascular EVTs. Blue = PD-L1, purple = HLA-G, yellow = CD56, grey = H3. **g.** Inset of **c**, showing decidual stromal cells (fibroblasts) and macrophages. Blue = CD163, cyan = CD206, yellow = CD11c, grey = H3, red = vimentin. **h.** Cell lineage assignments overlaid onto the cell-segmentation output to produce a cell phenotype map.

macrophage ($CD14^+$) populations, ubiquitously co-expressing CD163 and CD206, consistent with an M2-polarized, tolerogenic phenotype[38] (Fig. 2g). In line with previous work showing pregnancy-specific recruitment, 77% of macrophages expressed DC-SIGN[39] (Fig. 2a). We further classified DC-$SIGN^+$ macrophages into three subsets (Mac2a, 2b, 2c) based on expression of CD11c (Mac2b, 2.7% of macrophages) or absence of HLA-DR (Mac2c, 10.3% of macrophages). The majority (64%) of macrophages were $CD11c^-$HLA-$DR^+$ (Mac2a). Macrophages lacking DC-SIGN (23% of macrophages) were further categorized based on CD68 expression ($CD68^-$ Mac1b and $CD68^+$ Mac1a) (Fig. 2a, b).

Four subsets of NK cells ($CD3^-CD56^+$) were identified based on combinatorial co-expression of CD57, CD11c, and CD8. NK1 ($CD57^-CD16^{low}$) were the largest NK cell population present, making up 59.7% of NK cells (Fig. 2a, b). The remaining three subsets could be distinguished based on expression of CD57 (NK2, 25.8% of NK cells), CD11c (NK3, 11.3% of NK cells), or CD8 (NK4, 3.2% of NK cells) (Fig. 2a, b). T cells consisted of $CD8^+$ (53.2% of T cells), $CD56^+$ NKTs (28.8% of T cells), $CD4^+$ (17.1% of T cells), and sparse numbers of regulatory T (Treg) cells ($CD4^+FOXP3^+$, 0.7% of T cells); while no B cells were observed (Fig. 2a, b). Fetal cells (12.6% of all cells) primarily comprised four subsets of EVTs that were delineated based on combinatorial expression of HLA-G, CK7, CD57, and CD56 (Fig. 2a). HLA-$G^+$ interstitial EVT populations were $CK7^+$ (EVT1a, 44.6% of fetal cells), $CK7^-$ (EVT1b, 35.3% of fetal cells), or $CD56^+$ (EVT1c, 6.9% of fetal cells) (Fig. 2c-f). EVT2 lacked HLA-G and were $CD57^-CK7^{low}$ (EVT2, 9.4% of fetal cells). Notably, placental macrophages (Hofbauer cells) located in chorionic villi constituted the remainder (4.1%) of fetal cells and exhibited a cellular phenotype similar to that of Mac2c (DC-$SIGN^+$HLA-$DR^-$) decidual macrophages (Fig. 2a).

As previously reported, we detected IDO-1 expression in glandular cells[29], but also in vascular endothelium, where it has been previously reported to be scarce (12.3% of endothelial cells were IDO-$1^+$, Fig. 2a)[34]. Our analysis revealed numerous functional subsets of maternal cells, including TIM-$3^+$Galectin-$9^+$, $iNOS^+$, and HO-$1^+$ subsets of DC-$SIGN^+$ macrophages, Galectin-$9^+$ fibroblasts (36.7% Galectin-$9^+$, Fig. 2d), and an intriguing TIM-$3^+Lck^+$ subset of Tregs that accounted for >50% of this population (Fig. 2a, b). Interestingly, both Tregs and NKT cells were highly proliferative (13.7% $Ki67^+$ Tregs,

17% Ki67$^+$ NKT cells), and with the notable exception of CD8$^+$ NK cells (22.9% GrB$^+$), had higher frequencies of GrB (Granzyme B) expressing cells than any NK cell subset (33.7% GrB$^+$ NKT, 19.5% GrB$^+$ Treg). Our highly multiplexed imaging platform confirmed prior findings[32,39–41] and enabled us to enumerate an ensemble of functional states across multiple lineages that were collectively consistent with maintaining a tolerogenic niche.

## SAR progression is tightly correlated with the local tissue microenvironment

Perfusion of the intervillous space by uterine spiral arteries is the sole source of oxygen and nutrients to the growing fetus after the establishment of arterial flow. During the first half of pregnancy, these vessels undergo an extensive remodeling process that culminates in dilated, non-contractile vessels depleted of smooth muscle and where the maternal endothelium has been replaced by EVTs. While abnormal SAR is associated with obstetric complications, such as intrauterine growth restriction and preeclampsia[12,13], it is still not fully understood which cell populations directly participate in SAR, how this process is locally regulated, and to what extent these changes are synchronized with GA.

We therefore used our spatiotemporal atlas of decidua to construct a SAR trajectory to reveal how this process relates to temporal changes in decidua cell composition and structure. Using artery size, smooth muscle layer disruption and loss, endothelial continuity, EVT infiltration, and EVT endothelization to determine the extent of SAR, we manually assigned each artery to one of five sequential remodeling stages based on previously published criteria[42] (Fig. 3a). To ensure scoring was not biased by patient demographics, the score of neighboring arteries, or the composition of nearby stroma, scoring was performed on cropped images of each artery independently by blinded experts. Out of 588 arteries, 186 were unremodeled and assigned to Stage 1 (Fig. 3b, c). Stage 2 arteries (300 arteries) were characterized by moderate smooth muscle disruption and endothelial swelling (Fig. 3d, e). Stage 3 arteries (43 arteries) exhibited more dilation, smooth muscle loss, and early endothelial disruption (Fig. 3f, g). Progression to Stage 4 (34 arteries) was marked by the presence of EVTs within the arterial lumen (Fig. 3h,i), while fully remodeled Stage 5 arteries (25 arteries) were identified based on their very large size, near-complete smooth muscle loss, and EVT endothelization (Fig. 3j, k, see Methods, Extended Data Fig. S3a, Supplementary Table

5).

Although SAR correlated with GA to some extent (Spearman's $\rho$=0.28, p-value = $1.5*10^{-12}$), in many cases artery staging and GA were discordant. For example, at least one late-stage artery (Stage 4-5) was present in 40% of week 8 samples, while minimally remodeled arteries were present throughout (Fig. 3l). Moreover, SAR staging of arteries from the same patient often varied significantly between tissue cores (32% of patients had arteries that differed by at least two stages), suggesting that this discordance could be highlighting aspects of SAR that are locally regulated by the tissue microenvironment (Fig. 3l, Extended Data Fig. S3b).

This decoupling of SAR and GA permitted us to identify changes in decidual composition that were predominantly driven by one or the other. We first developed a quantitative staging scheme for assigning a continuous, quantitative, and accurate remodeling score in an automated fashion. For each artery, we extracted 35 parameters describing the same aspects of arterial morphology that were used for manual scoring (Fig. 3m, see Methods, Extended Data Fig. S3d). Together with manual staging, we used this quantitative morphologic profile to construct a highly resolved pseudotime trajectory of SAR using linear discriminant analysis (LDA)[43] (Fig. 3m, n). We generated this trajectory by combining the 35 morphological features with our manually defined stage labels and applying LDA to project each artery with respect to a two-dimensional LDA space in which separation of arteries by their manually assigned stages is optimal (see Methods). This separation was mainly driven by artery shape and size, properties of the smooth muscle layer and EVT presence (see Methods, Supplementary Table 6).

We then defined a remodeling trajectory as the polynomial fit to artery points in this space and subsequently mapped each artery ($a_i$) to the nearest point along this curve ($b_i$, Fig. 3n inset, see Methods). Finally, a remodeling score ($\delta$) was determined by calculating the distance along this curve from the point of origin ($x_o$) to $b_i$ for each artery (See integral in Fig. 3n, Extended Data Fig. S3e, f, Supplementary Table 5). With our continuous remodeling score $\delta$, we next defined a simple scheme to differentiate GA- and SAR-driven trends by performing linear regressions of cell frequency per image both as a function of GA and as a function of $\delta$. Regression $R^2$ and p-values were used as proxies for trend

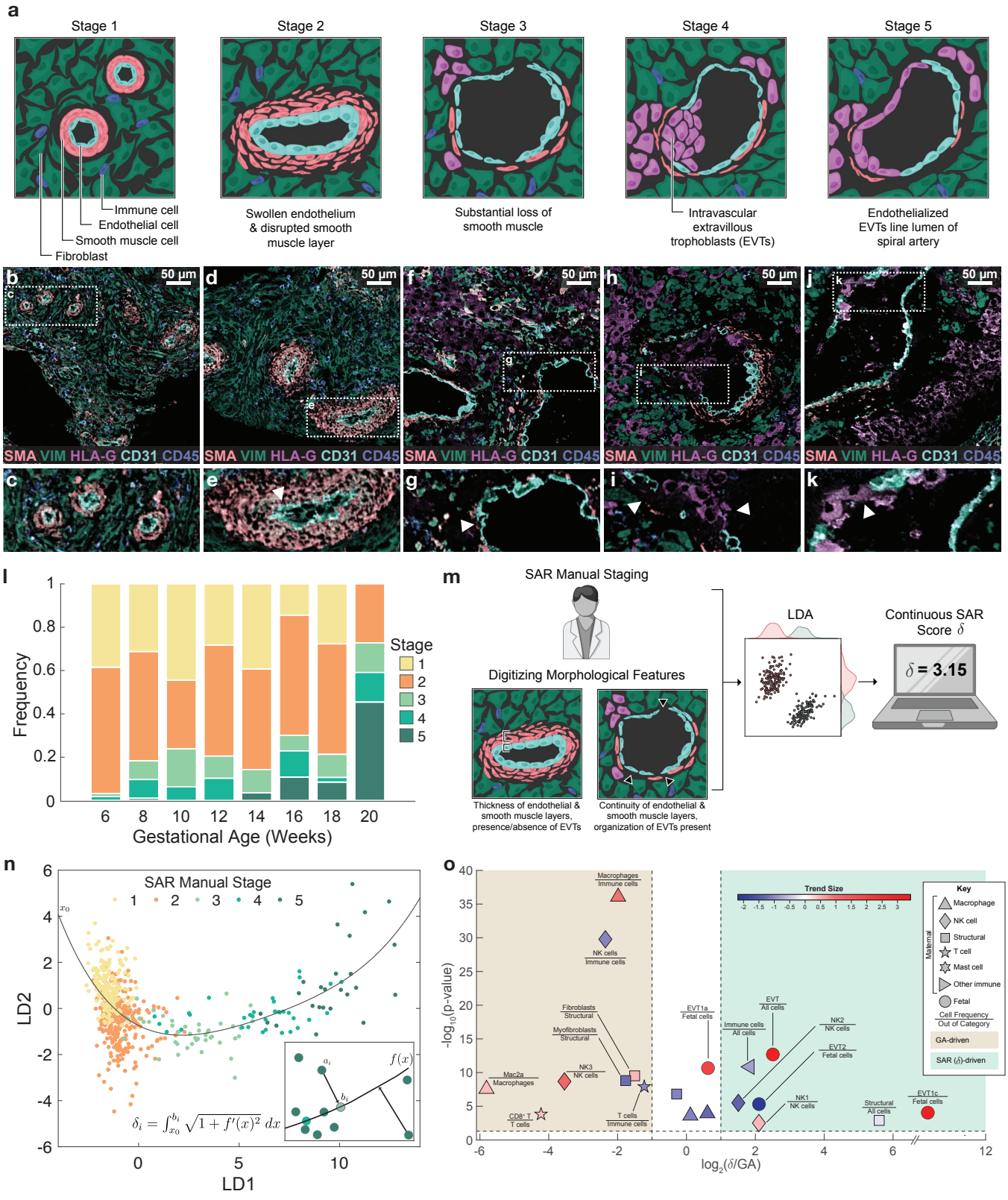

**Figure 3 | Spiral Artery Remodeling (SAR) progression significantly influences maternal-fetal interface composition. a.** Diagram showing key characteristics of SAR Stages 1-5, assessed manually. **b.** Representative MIBI color overlay of SAR manual Stage 1 arteries. VIM, vimentin; SMA, smooth muscle actin. **c.** Inset of **b**, showing SAR manual Stage 1 arteries. **d.** Representative MIBI color overlay of SAR manual Stage 2 arteries. **e.** Inset of **d**, showing one SAR manual Stage 2 artery. Arrowhead; swollen endothelial cells. **f.** Representative MIBI color overlay of SAR manual Stage 3 arteries. **g.** Inset of **f**, showing one SAR manual Stage 3 artery. Arrowhead; substantial loss of smooth muscle **h.** Representative MIBI color overlay of one SAR manual Stage 4 artery. **i.** Inset of **h**, showing one SAR manual Stage 4 artery. Arrowheads; intravascular EVTs. **j.** Representative MIBI color overlay of one SAR manual Stage 5 artery. **k.** Inset of **j**, showing one SAR manual Stage 5 artery. Arrowhead; endothelialized intravascular EVTs lining the spiral artery lumen. **l.** Distribution of SAR manual stages by gestational age (GA). **m.** Schematic of calculating the continuous SAR remodeling score ($\delta$). Manual stages along with quantified digitized morphological features were used to construct a trajectory of SAR using LDA from which the continuous SAR score $\delta$ was calculated. **n.** Scatter of arteries in LDA space color coded by manually assigned stage. The polynomial fit depicts the remodeling trajectory. Inset: matching each artery point $a_i$ to the SAR trajectory by finding the nearest point along trajectory $b_i$. The continuous SAR score $\delta$ was then defined as the distance from origin $x_0$ to $b_i$ along the trajectory curve. **o.** Volcano plot distinguishing GA-driven from SAR ($\delta$)-driven cell-type frequencies. X axis: $\log_2$ ratio of $R^2$ derived from linear regression against SAR ($\delta$) and GA. Y axis: $-\log_{10}$ of the p-value for the better-fitting regression model. Points are color coded by the trend size observed in the better-fitting regression model.

quality and to assess significance, respectively. Trends where $R^2$ for GA and SAR differed by at least two-fold were classified as being driven predominately by a single process, while ones falling below this cutoff were classified as synchronized (Fig. 3o, see Methods, Extended Data Fig. S3g, h, Supplementary Table 7).

Consistent with previous studies reporting fewer interstitial EVTs in pregnancy complications that were related to impaired SAR, EVT decidual presence was better correlated with SAR than with GA ($Log_2$ $R^2$ ratio(δ:GA) = 2.5, p-value for δ =$1e^{-13}$). This increase in decidual EVTs with SAR was accompanied by a decrease in immune and structural cell frequencies (Fig. 3o). Within the EVT compartment, the frequency of EVT1c out of fetal cells exhibited the greatest bias for SAR ($Log_2$ $R^2$ ratio(δ:GA) = 10.3, p-value for δ = $9e^{-4}$, increase of 2.8 times the mean value, Fig. 3o), further highlighting this dependence. Changes in the relative proportion of cell types within the immune compartment were mostly driven by GA (Fig. 3o). Notably, the DC-SIGN$^+$ Mac2a subset which was previously reported to be pregnancy-specific[39] was heavily GA-biased ($Log_2$ $R^2$ ratio(δ:GA) = -5.8, p-value for GA = $3e^{-8}$, Fig. 3o), suggesting that this population is recruited in a manner that is agnostic to SAR. In contrast, the trade-offs within the NK cell compartment where the relative proportion of NK2 (CD57$^+$) diminished as NK1 (CD57$^-$) increased were SAR-dependent ($Log_2$ $R^2$ ratio(δ:GA) ≥ 1.5, p-value for δ ≤ 0.003, Fig.

3o). Interestingly, CD57 expression in human NKs results in a highly cytotoxic phenotype and has been shown to play a pivotal role in cancer immunosurveillance[44]. These trends suggest that during pregnancy, the reduction in cytotoxic mature NKs promotes a permissive niche where EVTs can invade and initiate SAR.

## A lymphoid to myeloid shift in immune compartment composition is tightly correlated with GA

Our analyses indicated a robust, GA dependent shift from a lymphoid to myeloid dominated immune landscape, characterized by fewer NK and T cells and a concomitant

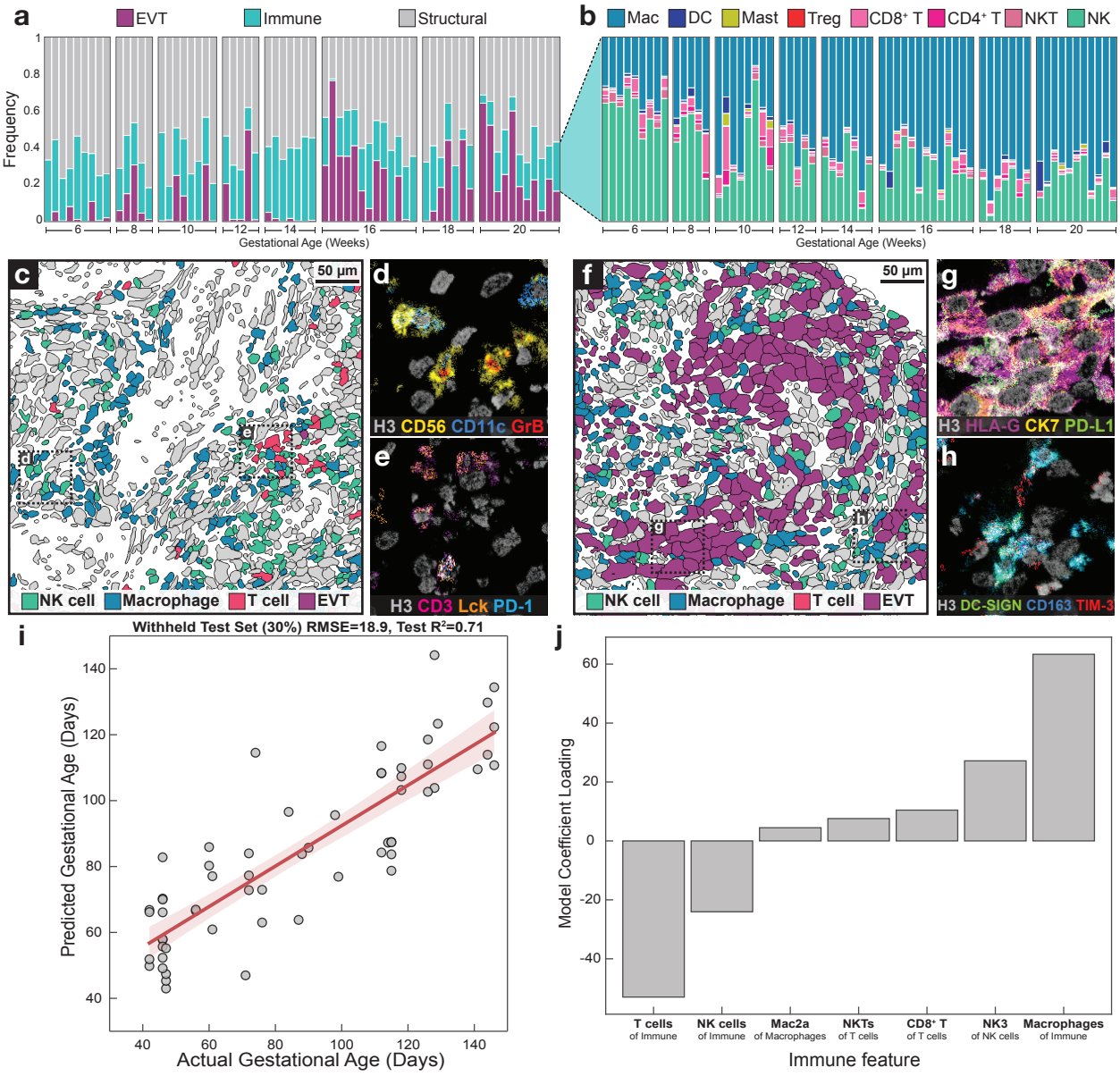

**Figure 4 | A lymphoid-to-myeloid shift in immune-compartment composition is tightly correlated with gestational age (GA). a.** Frequency of EVT, immune, and structural cell populations per patient, with patients ordered by GA. **b.** Frequency of immune cell populations per patient, by GA. MAC, macrophage; NKT, NK T cells; NK, total NK cells. **c.** Representative cell phenotype map of immune composition in decidual tissue in an early (6 weeks GA) sample. Green = NK, blue = macrophage, pink = T cell, purple = EVT, grey = other. **d.** Inset of **c**, showing a MIBI color overlay of NK cells with GrB expression. Grey = H3, yellow = CD56, blue = CD11c, red = GrB. **e.** Inset of **c**, showing a MIBI color overlay of T cells with PD-1 and Lck expression. Grey = H3, pink = CD3, orange = Lck, blue = PD-1. **f.** Representative cell phenotype map of immune composition in decidual tissue in a late (16 weeks GA) sample. Green = NK, blue = macrophage, pink = T cell, purple = EVT, grey = other. **g.** Inset of **f**, showing a MIBI color overlay of EVTs (1a, 1b) with PD-L1 expression. Grey = H3, purple = HLA-G, yellow = CD56, green = PD-L1. **h.** Inset of **f**, showing a MIBI color overlay of macrophages with TIM-3 expression. Grey = H3, green = DC-SIGN, blue = CD163, red = TIM-3. **i.** Predicted versus actual GA in days for a ridge regression model trained on GA-associated immune features, for a withheld test set (30%). Shaded region; 1 standard deviation. **j.** Ridge regression model coefficient loadings for GA-associated immune features.

increase in macrophage frequency ($Log_2$ $R^2$ ratio(δ:GA) ≤ -1.2, p-value for δ ≤ $1.2e^{-8}$, Figs. 3o, 4a, b). In MIBI images at weeks 6-8 (Fig. 4c, e), show NK cells and T cells, including those exhibiting cytotoxic (Fig. 4d) and immunosuppressive (Fig. 4e) phenotypes, greatly outnumbered macrophages of all subsets (Fig. 4b, c). Contrastingly, images from weeks 16-20 were dominated by interstitial EVTs (Figs. 4a, 4f-g) and an accompanying increase in tolerogenic macrophage populations (Fig. 4h) in relation to NK and T cells. To further evaluate this relationship, we asked whether immune cell composition in the decidua alone could be used to predict GA. Selecting immune features that were found to be preferentially associated with GA rather than SAR (Fig. 3o), we trained and validated a ridge regression model on a per-image basis using a random 70/30 test-train split (Extended Data Fig. S4a). Remarkably, the trained model predicted GA in the withheld test set within 19 days of the ground-truth value ($R^2$=0.7, Fig. 4i). On inspecting the model weights, we found that the relative contribution of decidual immune cells was consistent with the observed shift in the proportion of myeloid and lymphoid cells. In particular, the relative frequencies of T and NK cells were negatively correlated with GA, while total macrophage frequency was positively correlated with GA (Fig. 4j). Notably, a modified regression model for predicting SAR (δ) based on the same immune cell population parameters performed poorly ($R^2$=0.05, RMSE=0.85, Extended Data Fig. S4b), reinforcing our hypothesis that these immune correlates are driven by GA and not SAR.

## Coordinated up-regulation of tolerogenic functional markers with GA

Having examined the influence of GA and SAR in driving changes in the frequency

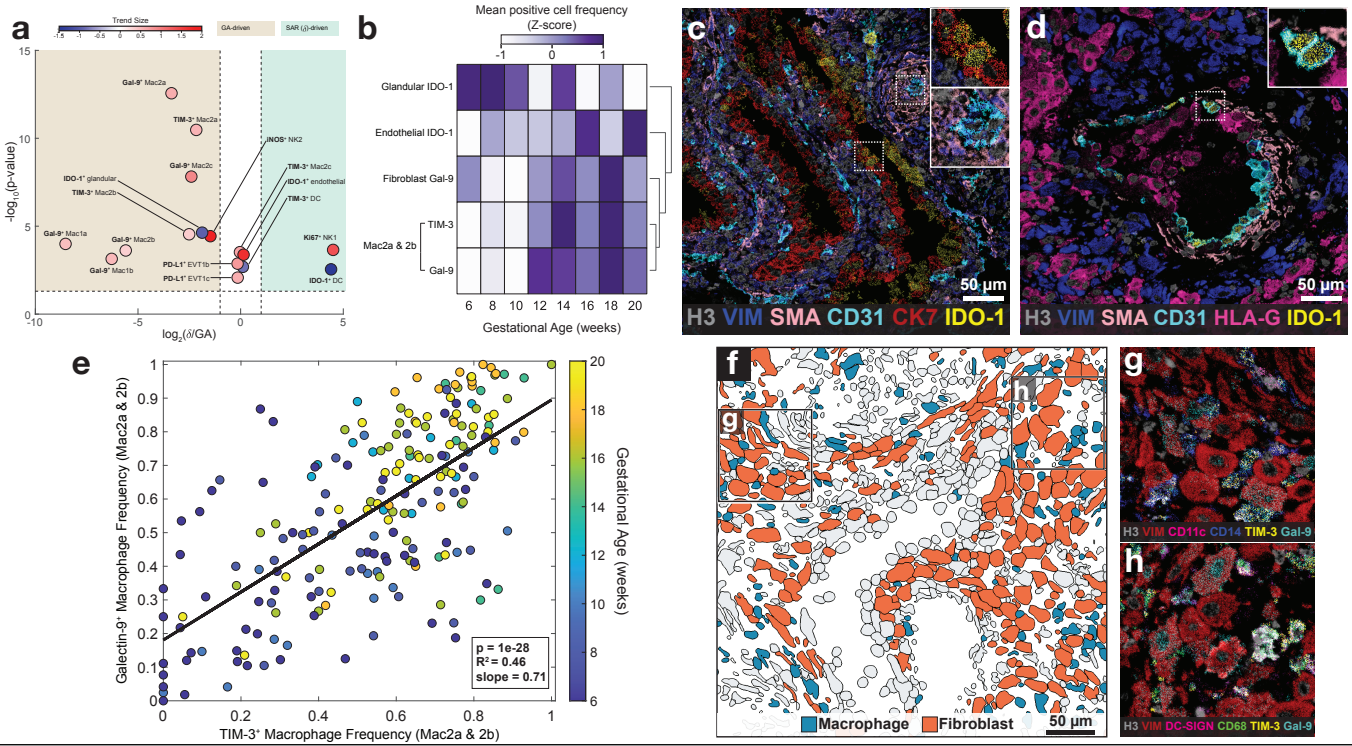


**Figure 5 | Coordinated up-regulation of tolerogenic functional markers with gestational age (GA). a.** Volcano plot distinguishing GA-driven from SAR ($\delta$)-driven cell type-specific functional marker positivity fraction. X axis: $\log_2$ ratio of trend size is a relative measurement of $R^2$ derived from linear regression against GA or SAR ($\delta$) and GA. Y axis: $-\log_{10}$ of the p-value for the better-fitting regression model. Points are color coded by the trend size observed in the better-fitting regression model **b.** Heatmap of changes in a subset of GA-driven functional markers as a function of GA in weeks. **c.** MIBI color overlay of IDO-1 expression in glandular cells (top inset) and endothelial cells (bottom inset) in an early (6 weeks GA) sample. Grey = H3, blue = VIM (vimentin), peach = SMA (smooth muscle actin), cyan = CD31, red = CK7, yellow = IDO-1. **d.** MIBI color overlay of IDO-1 expression in endothelial cells (inset) in spiral artery (SAR manual Stage 4) of a late (16 weeks GA) sample. Grey = H3, blue = vimentin, peach = SMA, cyan = CD31, magenta = HLA-G, yellow = IDO-1. **e.** Per-image Mac2a and Mac2b TIM-3$^+$ cell frequency versus Mac2a and Mac2b galectin-9$^+$ frequency, colored by GA. **f.** Cell phenotype map of macrophages and decidual fibroblasts. **g.** Inset of **f**; MIBI color overlay of TIM-3$^+$ and galectin-9$^+$ Mac2b and fibroblast cells. **h.** Inset of **f**; MIBI color overlay of TIM-3$^+$ and galectin-9$^+$ Mac1a, Mac1b, Mac2a, and fibroblast cells. Grey = H3, red = vimentin, pink = DC-SIGN, green = CD68, yellow = TIM-3, turquoise = Galectin-9.

of cell populations in the decidua, we next employed a similar approach to understand how these two time axes correlate with shifts in decidual function. Using the same method as our analysis of cell frequencies, we classified the temporal dynamics of functional markers expression as GA-driven, SAR-driven, or synchronized (comparably correlated with both GA and SAR) (Fig. 3o). Out of the 48 cell population-functional marker combinations that were evaluated, 16 exhibited functional marker expression that significantly correlated with one or both of these axes (Fig. 5a, see Methods, Supplementary Table 8). These data revealed three overarching trends. First, both SAR

and GA are associated with dynamic changes in IDO-1 expression. For example, we identified a GA-driven decline in IDO-1$^+$ glandular cells ($Log_2$ $R^2$ ratio(δ:GA) = -1.8, p-value for GA = $2.3e^{-5}$), a SAR-driven decline in IDO-1$^+$ dendritic cells ($Log_2$ $R^2$ ratio(δ:GA) = 4.4, p-value for δ = $3e^{-3}$), and an increase in IDO-1$^+$ vascular endothelium (p-value = $4e^{-4}$ ,Fig. 5c, d) that was comparably correlated with both GA and SAR (Fig. 5b, d). Second, consistent with the cell frequency analysis (Fig. 3o) in which NK1 exhibited a frequency increase preferentially associated with SAR, NK1 also exhibited a SAR dependent increase in Ki67$^+$ frequency ($Log_2$ $R^2$ ratio(δ:GA) = 4.5, p-value for δ = $2e^{-4}$) becoming more proliferative as arterial remodeling progresses (Fig. 5a). Third, functional shifts in innate immunity were preferentially correlated with GA. All five macrophage populations upregulated either TIM-3 and/or its cognate ligand Galectin-9 with GA (Fig. 5a, b). This trend was most prominent in the Mac2a and Mac2b populations, where a tightly correlated up-regulation of both TIM-3 and Galectin-9 occurred (Fig. 5e-h, Extended Data Fig. S5a). Interestingly, Galectin-9 upregulation was also detected in fibroblasts (Fig. 5b, f-h). Notably, TIM-3 and Galectin-9 have been implicated in suppressing anti-tumor surveillance by impairing the activity of cytotoxic NK and T cells in various human cancers[30,45–47]. Taken with the SAR-driven decline in the proportion of the cytotoxic NK2 observed here (Fig. 3o), these findings may suggest that TIM-3$^+$ Galectin-9$^+$ macrophages are serving a similar tolerogenic role in decidua.

## Spatio-temporal EVT distribution suggests that intravasation is the predominant route of EVT invasion in superficial decidua

Although intravascular EVTs are known to originate from the cytotrophoblast cell columns, their path of migration remains a subject of debate primarily revolving around two models: intravasation and extravasation (Fig. 6a). In the intravasation model, EVTs detach from the cell columns and migrate through the decidua to first localize around the spiral arteries. These perivascular EVTs then enter spiral arteries by migrating through the arterial wall. In contrast, in the extravasation model, EVTs do not traverse the arterial wall from within the decidua. Instead, detaching EVTs migrate retrograde against arterial blood flow after entering at the basal plate where spiral arteries empty and merge into the intervillous space[9].

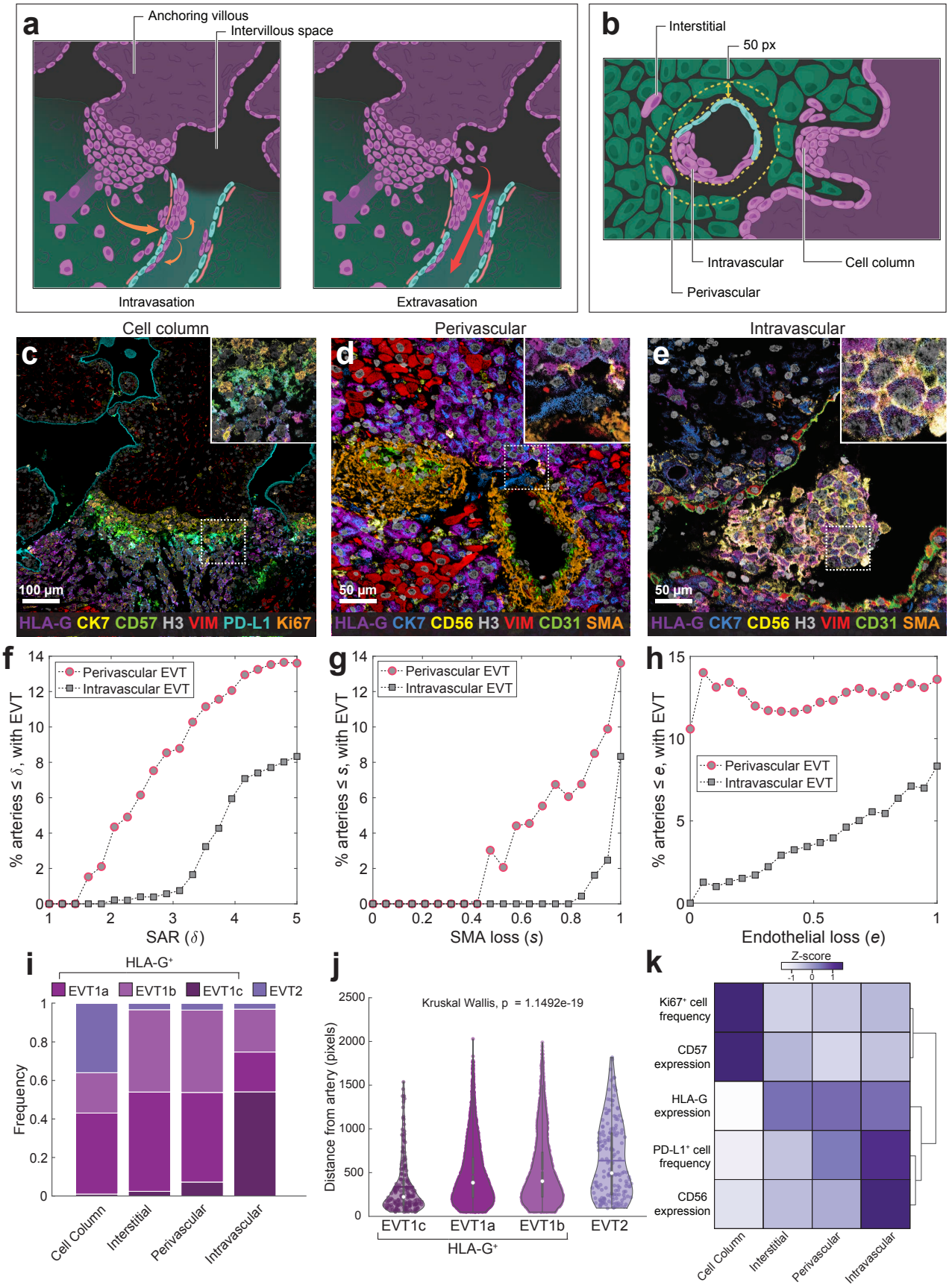

**Figure 6 | Spatiotemporal EVT distributions suggest that intravasation is the predominant route of EVT invasion in superficial decidua. a.** Two hypotheses for intravascular EVT invasion. (Left) Intravasation: orange arrows indicate movements of EVTs from the cell column of the anchoring villi into the decidua and through the wall of the artery and into the lumen. (Right) Extravasation: red arrows indicate movement of EVTs from the fetal villi through the intervillous space into the artery. **b.** Anatomical locations of interstitial, intravascular, perivascular, and cell column EVT populations in the decidua. **c.** MIBI overlay of anchoring villous and associated cell column EVT populations. Inset: cell column EVTs. Purple = HLA-G, yellow = CK7, green = CD57, grey = H3, red = VIM (vimentin), cyan = PD-L1, orange = Ki67 **d.** MIBI overlay of spiral arteries and associated perivascular EVT populations. Inset: perivascular EVT breaching artery wall. Purple = HLA-G, blue = CK7, yellow = CD56, grey = H3, red = VIM, green = CD31, orange = SMA (smooth muscle actin). **e.** MIBI overlay of remodeled spiral arteries and associated intravascular EVT populations. Inset; intravascular EVTs in a clump. Purple = HLA-G, blue = CK7, yellow = CD56, grey = H3, red = VIM, green = CD31, orange = SMA. **f.** Percentage of arteries with scores less than or equal to a given SAR ($\delta$) threshold, by perivascular or intravascular EVTs present. **g.** Percentage of arteries with scores less than or equal to a given SMA loss (s) threshold, by perivascular or intravascular EVTs present. **h.** Percentage of arteries with scores less than or equal to a given endothelial loss (e) threshold, by perivascular or intravascular EVTs present. **i.** Frequency of EVT populations by anatomical location. **j.** Violin plot of distance from artery (in pixels) of EVTs grouped by EVT type. **k.** Heatmap of lineage and functional marker trends of EVT populations by anatomical location. Lineage marker (CD57, HLA-G, CD56) trends are mean expression values of EVT populations. Functional marker (Ki67, PD-L1) trends are the mean positive cell frequencies of EVT populations. Rows are z-scored and hierarchically clustered.

To determine which model best explains arterial invasion, we used our spatio-temporal atlas to quantify how the phenotype and spatial distribution of EVTs evolve with respect to SAR. First, we manually defined feature masks demarcating cell column anchoring villi and three decidual compartments—interstitial, perivascular, and intravascular in our images (Fig. 6b) —to quantify EVT frequency in each (Fig. 6c-e). Together with our SAR temporal trajectory, we used these data to ask a question that has been qualitatively explored in previous work[20]: Where do EVTs accumulate first—in the perivascular compartment (directly proximal to arteries) or within the intravascular compartment? We quantified peri- and intravascular EVTs on a per-artery basis with respect to their remodeling score δ and found that perivascular EVTs began accumulating around less remodeled arteries in the decidua (Fig. 6f) and were consistently present at earlier remodeling stages than intravascular EVTs (median δ = 2.2 vs. 3.2, Kruskal-Wallis p-value = $5e^{-8}$, Extended Data Fig. S6a). For arteries in which both were present, the $Log_2$ ratio of EVTs present in these two compartments followed a continuous and smooth trend as remodeling progressed, with intravascular EVTs increasing at the expense of perivascular EVTs ($R^2$ = 0.5, p-value = $9e^{-12}$, Extended Data Fig. S6b). For a small number of arteries, we observed perivascular EVTs breaching the artery wall, suggesting they are in the process of invading the arterial lumen (Fig. 6d). These data are more

consistent with the intravasation model in which perivascular EVT are necessary before intravascular EVT could appear.

Loss of smooth muscle and endothelium have defining roles in determining the extent of SAR. Using morphometrics to quantify the extent of these concentric layers of the arterial wall (see Methods), we examined how their integrity relates to EVT enrichment in the perivascular and intravascular compartments. Similar to the trend seen with respect to remodeling score δ, accumulation of perivascular EVTs was consistently present around arteries at an earlier stage, with intravascular EVTs only appearing after 80% smooth muscle loss (median smooth muscle loss for arteries with at least five intravascular EVT present: 98%, Fig. 6g). Perivascular EVTs were present around arteries irrespective of the degree of endothelium loss, while intravascular EVTs increased with endothelium loss (Fig. 6h, linear regression on Log transformed intravascular EVT as a function of endothelium loss: $R^2$=0.13, p-value =$3e^{-4}$) indicating that endothelial disruption is a precursor to EVT entry into the arterial lumen. This conclusion further supports the intravasation model, in which EVTs must transverse the endothelial barrier to enter the arterial lumen.

Taken together, these data are consistent with a sequential process in which EVTs detach from the cytotrophoblast cell columns and migrate through the decidua as interstitial EVTs in order to accumulate in the perivascular compartment prior to intravasation, as suggested previously[20]. To further evaluate this model, we posed the following questions: Does EVT phenotype shift in a progressive manner that is consistent with this stepwise intravasation model? If so, do intravascular EVTs more closely resemble the cell column or perivascular compartment?

To answer these questions, we first compared the frequencies of the four EVT cell populations within cell column, interstitial, perivascular, and intravascular masks. The composition of each of these compartments shifted in a systematic manner along the proposed path of migration: the cell columns consisted primarily of EVT1a, EVT1b and EVT2 subsets with few $CD56^+$ EVT1c cells (99% vs. 1%). In the interstitial compartment, the frequency of EVT2 dropped by 11-fold while the frequency of EVT1c cells increased modestly to 2.4%. EVT1c cells were further enriched within the perivascular compartment

(7.3%) but were most prevalent in the intravascular compartment (54%, Fig. 6i). In addition, EVT1c cells were found significantly closer to arteries than EVT2 cells (Kruskal Wallis p-value = $1.15e^{-19}$, Fig. 6j).

Comparison of functional marker expression across all subsets within each masked compartment, again revealed a progressive shift in EVT phenotype that best aligned with a route of invasion consistent with an intravasation model. Cell column compartments were uniquely enriched for proliferative ($Ki67^+$), $CD57^+$ EVTs (Fig. 6k). With decidual EVT invasion, a precipitous drop in CD57 and Ki67 expression was accompanied by a progressive increase in PD-L1 that peaked in the intravascular compartment (Fig. 6k). Notably, the intravascular compartment most closely resembled the perivascular compartment in terms of functional marker expression (Fig. 6k, perivascular 9.4% closer than interstitial to intravascular, Kruskal-Wallis p-value = $8e^{-7}$, see Methods, Extended Data Fig. S6c). While the perivascular compartment is the most similar to the intravascular compartment, a noticeable difference between the two compartments was driven by PD-L1 and CD56 expression levels (Fig. 6k). This difference stems from the highest prevalence of the $CD56^+$ $PDL\text{-}1^+$ EVT1c cells in the intravascular compartment, which further increases with SAR (Fig. 6i, Extended Data Fig. S6d-f).

One potential explanation for the steep increase in EVT1c prevalence between the perivascular and intravascular compartment is that arterial intravasation of perivascular EVTs is accompanied by upregulation of CD56, such that EVT1a-b subsets would effectively become the EVT1c subset. We therefore hypothesized that such a process would involve an intermediate state between the two in which the EVT1a-b subsets moderately express of CD56 en-route to the high expression observed in the EVT1c subset. To test this hypothesis, we compared the average CD56 intensity of perivascular and intravascular EVT1a-b EVTs on a per-artery basis (for arteries that initiated remodeling: $\delta \geq 2$). This analysis detected a statistically significant increase in CD56 expression between the perivascular and intravascular compartment by EVT1a-b subsets (sided Wilcoxon signed rank test p-value = $5e^{-3}$, Extended Data Fig. S6g). An alternative explanation for the disproportionate enrichment of EVT1c within vessels is that they are more proliferative. However, only 0.5% of intravascular EVT1c were $Ki67^+$ compared to 9.6% and 1.8% of intravascular EVT1a and EVT1b cells, respectively (Fig. 6k, Extended

Data Fig. S6h).

Note that given the observational nature of our spatiotemporal atlas, neither model can be definitively ruled in or out. However, taken together these analyses best align with an intravasation model in which decidual invasion of cell column EVTs is accompanied by pronounced downregulation of CD57 and Ki67 and upregulation of HLA-G. Perivascular accumulation of EVTs occurs early in SAR, preceding the appearance of intravascular EVTs and any loss in endothelium. In this model, as the endothelial barrier is lost, perivascular EVTs invade the artery lumen and upregulate CD56.

# Discussion

Decidualization is a fascinating process with no other normative precedent in human biology, where the structure and function of the maternal endometrium transforms to promote invasion of actively dividing, genetically dissimilar placental cells. Many aspects of this process are primate-specific and some, such as deep arterial invasion of EVTs into the myometrium, are thought to be largely restricted to humans with some evidence in great apes[14–17,48]. Given this lack of tractable and relevant animal models and the inability to study decidualization prospectively, our understanding of this process is immature relative to other areas of human physiology. With this in mind, we used MIBI-TOF and archival human tissue to generate the first spatiotemporal atlas of the maternal-fetal interface during 6-20 weeks gestation. The central focus of our study was to understand how global, temporally dependent changes in decidual composition are coupled to local regulation of vascular remodeling in pregnancy. While initial invasion of placental EVTs is prompted by a shift towards a permissive milieu, progression of SAR is dependent on subsequent migration and perivascular accumulation of EVTs, where they are thought to participate in cooperative cell-cell interactions with maternal fibroblasts, NK cells, and macrophages[4,5]. Thus, formation of the maternal-fetal interface is mediated by global, temporally dependent queues that serve as a gating function for remodeling processes that are regulated in the local tissue microenvironment.

With this paradigm in mind, we set out to delineate which aspects of the first half of pregnancy are driven globally by GA and how this relates to SAR. To achieve this, we

mapped the spatial distribution, composition, and functional state of ~500,000 maternal cells and fetal EVTs with respect to glands, anchoring cell column villi, and spiral arteries in >200 images from 66 patients. Using LDA, image morphometrics, and expert annotations, we assigned quantitative remodeling scores to every spiral artery in these images. We then examined how cell frequency and function changed with respect to GA and SAR. Our analysis of these changes determined GA to be the predominant driver of maternal immune cell composition (Figs. 30, 4i, j). Progressive decreases in NK and T cells drive a transition at 12-14 weeks GA from a lymphoid to myeloid predominant decidua enriched for iNOS$^{+}$ NK cells, IDO-1$^{+}$ vascular endothelium, and DC-SIGN$^{+}$ macrophages that co-express TIM-3 and Galectin-9 (Figs. 4b, 5a, b). Notably, this relationship between immune composition and GA was robust enough to allow us to predict GA within 19 days based exclusively on immune population frequencies (Fig. 4i).

In contrast, all EVT subsets and only two maternal cell populations (NK1 and NK2) preferentially correlated with progression of SAR. Higher remodeling scores were correlated with more EVTs, more NK1s, and fewer NK2s. NK1 and NK2 primarily differ in that the latter express CD57—a marker associated with a cytotoxic phenotype. Higher proportions of presumptively more reactive NK2s early in SAR aligns well with previous studies that have suggested that decidual NKs initiate early disruption of arterial smooth muscle through secretion of GrB, MMP2, and MMP9[26,49]. Likewise, the proportional gains seen here as SAR progresses of less reactive NK1s and invasive EVTs are consistent with the tolerizing effects of HLA-G, which has been shown previously to decrease NK cell cytotoxicity and induce production of IL-6 and IL-8 via binding of HLA-G to KIR2DL4, LILRB1, and LILRB2[50,51]. Taken together, these data suggest that maternal and fetal cells play cooperative, interdependent roles with SAR transitioning through NK- and EVT-dependent phases.

We also examined a long-standing open question in the field: What is the path of migration taken by EVTs that invade spiral arteries? On comparing cellular compositions within cytotrophoblast cell columns of anchoring villi, decidua, and arteries, we found that the local EVT frequency and phenotype within these regions shifted in a sequential, coordinated manner consistent with an intravasation model in which EVTs within the decidua enter spiral arteries through the arterial wall. Given the observational nature of

this study, we note that we cannot definitively rule out an extravasation model in which EVTs migrate retrograde after entering spiral arteries directly at the basal plate. With this limitation in mind, in our model EVTs detaching from proliferative cytotrophoblast cell columns first invade the decidua and transition to a CD57- $CK7^{+}$ $HLA\text{-}G^{+}$ phenotype in our proposed model. In line with previous work demonstrating EVT expression of MMP2 and MMP9[52], these cells migrate through the decidua and accumulate around spiral arteries where they participate in removal of arterial smooth muscle. As this layer is depleted, perivascular EVTs disrupt the underlying vascular endothelium and invade the arterial lumen where they form multicellular clumps. Intravascular invasion is accompanied by EVT upregulation of CD56, a homophilic binding molecule that has been suggested to be necessary for heterotypic cell adhesion to endothelial cells[53]. Finally, these multicellular clumps in fully remodeled arteries recede and are partially replaced by trans-differentiated, endothelialized EVTs that have displaced the maternal endothelium.

Formation of the maternal-fetal interface is an organized and controlled invasive process that is sometimes viewed as a template for understanding invasive and immunosuppressive properties of tumors[54]. Both processes involve a genetically dissimilar invasive cell type (haploidentical EVTs vs. clonal, mutated cancer cells), extracellular matrix remodeling, and recruitment of a wide variety of tolerogenic immune cells, including M2 polarized macrophages and proliferating Tregs. The intersection of anchoring placental villi and maternal decidua morphologically resembles the invasive margin of carcinomas and contains trophoblast cells expressing high levels of immunomodulatory proteins and growth factors implicated in tumor severity including PD-L1, IDO-1, TIM3, Her2, and EGFR [30,45,55,56]. In addition to these phenotypic and structural similarities, recent work revealing mosaicism and clonal mutations in normal term placentas demonstrate that this phenotypic overlap is even manifest at a genomic level[57].

Overall, we anticipate that this spatio-temporal atlas of the early human maternal-fetal interface will provide a normative framework for elucidating etiological perturbations in maternal-fetal tolerance and SAR in pregnancy complications. Likewise, this work may also serve as a template for understanding how immune tolerance, tissue remodeling, and angiogenesis are aberrantly recruited and synergized during tumor progression. With this in mind, we plan in future studies to extend this comparative approach to archival

tissue from patients with preeclampsia, placenta accreta, and choriocarcinoma to further elucidate cellular interactions involved in regulating SAR and EVT invasion.

# Methods

## Retrospective cohort design

The study cohort comprised decidua tissue from archival formalin-fixed, paraffin embedded (FFPE) blocks, sampled after elective pregnancy terminations at the Women Options Center at Zuckerberg San Francisco General Hospital, an outpatient clinic located within a large public hospital affiliated with an academic medical center. Patients at this clinic reflect a diverse population. The clinic serves women in the Bay Area as well as referrals from California and out of state. While the patient population is predominantly low-income mainly Medi-Cal patients, women of all economic backgrounds are cared for at the clinic.

In the clinic, an ultrasound examination is performed to estimate GA, and medical history is taken and logged as Electronic Medical Records ('eCW' - electronic clinical works) or handwritten forms. A board-certified gynecologist reviewed medical records and specifically extracted the following details: age, ethnicity, body mass index, gravidity, parity, prior terminations, smoking, medications, HIV status, history of preeclampsia, chronic hypertension, diabetes mellitus, renal disease, autoimmune disease, multifetal pregnancy, and congenital anomalies (Supplementary Table 1). For procedures occurring at less <14 weeks GA, suction aspiration is routinely used. For procedures at >14 weeks GA, a combination of suction aspiration and grasping forceps is used. After the procedure, tissue samples are routinely sent to pathology.

## TMA construction

Regions of decidua with maternal spiral arteries, were cored and combined in two TMA blocks by an experienced technician. Where possible, blocks containing the decidua basalis were selected. Information on the histological characteristics of the blocks retrieved, including the presence of cell column anchoring villi, is located in Supplementary Table 2. The first TMA consisted of 205 cores (including three tonsil cores, one endometrium core and one myometrium core) of 1 mm in diameter; the second

559 contained 86 cores of 1.5 mm in diameter. High resolution scans of each core were
560 uploaded to the Stanford Tissue Microarray Database (URL: http://tma.im/cgi-
561 bin/home.pl), a collaborative internal platform for designing, viewing, scoring, and
562 analyzing TMAs. Sequential recuts of the main experiment were stained with H&E, to aid
563 in choosing the imaging regions of interest (ROIs) and analyzing data.

564 ## Antibody preparation

565 Antibody staining was validated as described previously[28,58–60] . Briefly, each
566 reagent was first tested using single plex chromogenic IHC using multiple positive and
567 negative FFPE tissue controls prior to metal conjugation. Antibodies were then
568 conjugated to isotopic metal reporters as described previously[28,58–61] with the exception
569 of biotin-conjugated anti-PD-L1, for which a metal-conjugated secondary antibody was
570 used. Performance of metal conjugated antibody reagents were then tested within the
571 complete MIBI-TOF staining panel, under conditions identical to those in the main study
572 and compared with representative single plex chromogenic IHC to confirm equivalent
573 performance. Representative stains and information for each marker can be found in
574 Extended Data Fig. 1a and Supplementary Table 9 respectively. After conjugation,
575 antibodies were diluted in Candor PBS Antibody Stabilization solution (Candor
576 Bioscience). Antibodies were either stored at 4°C or lyophilized in 100 mM D-(+)-
577 Trehalose dehydrate (Sigma Aldrich) with ultrapure distilled $H_2O$ for storage at −20°C.
578 Before staining, lyophilized antibodies were reconstituted in a buffer of Tris (Thermo
579 Fisher Scientific), sodium azide (Sigma Aldrich), ultrapure water (Thermo Fisher
580 Scientific), and antibody stabilizer (Candor Bioscience) to a concentration of 0.05 mg/mL.
581 Information on the antibodies, metal reporters, and staining concentrations is located in
582 Supplementary Table 9.

583 ## Tissue staining

584 Tissues were sectioned (4 μm in thickness) from tissue blocks on gold and
585 tantalum-sputtered microscope slides. Slides were baked at 70°C for 20 minutes followed
586 by deparaffinization and rehydration with washes in xylene (3x), 100% ethanol (2x), 95%
587 ethanol (2x), 80% ethanol (1x), 70% ethanol (1x), and dd$H_2O$ with a Leica ST4020 Linear
588 Stainer (Leica Biosystems). Tissues next underwent antigen retrieval was carried out by

submerging sides in 3-in-1 Target Retrieval Solution (pH 9, DAKO Agilent) and incubating them at 97°C for 40 minutes in a Lab Vision PT Module (Thermo Fisher Scientific). After cooling to room temperature slides were washed in 1x PBS IHC Washer Buffer with Tween 20 (Cell Marque) with 0.1% (w/v) bovine serum albumin (Thermo Fisher). Next, all tissues underwent two rounds of blocking, the first to block endogenous biotin and avidin with an Avidin/Biotin Blocking Kit (Biolegend). Tissues were then washed with wash buffer and blocked for 1 hour at room temperature with 1x TBS IHC Wash Buffer with Tween 20 with 3% (v/v) normal donkey serum (Sigma-Aldrich), 0.1% (v/v) cold fish skin gelatin (Sigma Aldrich), 0.1% (v/v) Triton X-100, and 0.05% (v/v) Sodium Azide. The first antibody cocktail was prepared in 1x TBS IHC Wash Buffer with Tween 20 with 3% (v/v) normal donkey serum (Sigma-Aldrich) and filtered through a 0.1 µm centrifugal filter (Millipore) prior to incubation with tissue overnight at 4°C in a humidity chamber. After the overnight incubation slides were washed for 2 minutes in wash buffer. The second day, the antibody cocktail was prepared as described (Supplementary Table 9) and incubated with the tissues for 1 hour at 4°C in a humidity chamber. After staining, slides were washed twice for 5 minutes in wash buffer and fixed in a solution of 2% glutaraldehyde (Electron Microscopy Sciences) solution in low-barium PBS for 5 minutes. Slides were washed in low-barium PBS for 20 seconds then, using a linear stainer, through 0.1 M Tris at pH 8.5 (3x), ddH2O (2x), and then dehydrated by washing in 70% ethanol (1x), 80% ethanol (1x), 95% ethanol (2x), and 100% ethanol (2x). Slides were dried under vacuum prior to imaging.

## MIBI-TOF imaging

Imaging was performed using a custom MIBI-TOF instrument with a Xe+ primary ion source, as described previously[28,61]. 222 808 x 808um Fields of View (FOVs) were acquired at approximately 600 nm resolution using an ion dose of 7nA*hr/mm$^2$. After excluding 11 FOVs that contained necrotic or non-decidual tissue, or consisted of duplicate tissue regions, the final dataset consisted of 211 FOVs from 66 patients.

## Low-level image processing

Multiplexed image sets were extracted, slide background-subtracted, denoised, and aggregate filtered as previously described[35,59–61]. For several markers, a

"background" channel consisting of signal from the mass 128 channel was used. All parameters used as inputs for low-level processing are listed in Supplementary Table 9.

## Feature annotation

Large tissue features were manually annotated in collaboration with a perinatal pathologist. Pseudo-colored MIBI images with H3 to identify cell nuclei, vimentin for decidual stromal cells, smooth muscle actin and CD31 for vessels, cytokeratin 7 (CK7) for glands and the fetal cell columns, and HLA-G for EVTs were used to guide annotation. Serial H&E sections, and an H&E recut of the entire block, if necessary, were additionally used to supplement annotation. Labelling was performed in ImageJ and the annotated features were exported as binary TIF masks.

## Single cell segmentation

The Mesmer segmentation algorithm[36] was adapted specifically to segment the cells in our dataset. First, training data were generated using a subset of 15 images out of 211 in our cohort, in addition to 10 decidua MIBI-TOF images from titration data. 1024 x 1024 pixel crops were selected to encompass the range of different cell morphologies present. The markers H3, vimentin, HLA-G, CD3, CD14 and CD56 were used to capture the major cell lineages present. Subsequently, a team of annotators parsed these images to identify the location of each unique cell using DeepCell Label, custom annotation software specifically developed for this task[36] (code URL: https://github.com/vanvalenlab/deepcell-label). The manually annotated images were used to generate partially overlapping crops of 256 x 256 pixels from each image. In total, training data included 1600 distinct crops with 93,000 cells. This dataset was used to retrain the Mesmer segmentation model, modifying the architecture to accept six distinct channels of input. The output from the network was then post-processed using the default model settings (Extended Data Fig. S2a).

## Segmentation post-processing

Examination of the images revealed that glandular cells and chorionic villus trophoblasts did not express any markers included in the training data; namely these cells were predominantly $CK7^{+}$. This resulted in effectively nuclear-only segmentation being

predicted by the CNN within these features. To account for this, segmented cells that overlapped with the gland mask were expanded radially by 5 pixels, and those in the cell column mask by 2 pixels. This approach accounted for glandular cells and cell column anchoring trophoblasts that were not expressing any markers but were included in the training data, resulting in effectively nuclear-only segmentation being predicted by the convolutional neural network. The number of pixels used for expansion was optimized to approximate the observed cell size, based on systematic inspection of three images per GA.

## Single-cell phenotyping and composition

Single cell expression data were extracted for all cell objects and area-normalized. Objects <100 pixels in area were deemed noncellular and excluded from subsequent analyses. Single-cell data were linearly scaled with a scaling factor of 100 and ArcSinh-transformed with a co-factor of 5. All mass channels were normalized to the 99th percentile. To assign decidual cell populations (≥ 70% cell area in decidua) to a lineage, the clustering algorithm FlowSOM (Bioconductor "FlowSOM" package in R)[37] was used, which separated cells into 100 clusters based on the expression of 19 canonical lineage defining markers (Extended Data Fig. S2b). Clusters were further classified into 21 cell populations, with proper lineage assignments ensured by manual examination of overlayed FlowSOM cluster identity with lineage-specific markers. Clusters containing non biologically meaningful or distinct signals were assigned the label 'other'. Tregs were identified by thresholding T cells (FlowSOM clusters 43, 53, 63) with CD3 signal ≥ the mean CD3 expression of $CD4^+$ T cells and > 0.5 normalized expression of FOXP3. Mast cells were identified as cells for which normalized expression of tryptase was >0.9. Mac2b ($CD11c^+$) cells were identified as macrophages with >0.5 normalized expression of CD11c. Placental macrophages (Hofbauer cells) were defined as $CD14^+$ >0.5 cells located within the cell column. Cells from FlowSOM clusters 4, 5, and 15 ubiquitously and predominantly expressed CK7 and were reassigned to the EVT2 subset if located within the cell column feature mask, or as glandular cells otherwise (Extended Data Fig. S2b). These thresholds were selected based on the distribution of lineage marker expression (Extended Data Fig. S2c) as well as on systematic examination of the images by eye

since expression patterns varied significantly between markers.

## Definition of thresholds for functional marker positivity

Cells were considered positive for a functional marker if their scaled expression level was ≥ a set threshold, as described previously[61]. Thresholds for individual functional markers were determined based on the distribution of functional marker expression and by examining the images by eye, as expression patterns varied significantly between markers (Extended Data Fig. S2e, Supplementary Table 4). To set the per marker thresholds, 5 images for each functional marker were reviewed and increasing threshold values were examined using custom software. Subsequently, cells defined as negative for a marker based on the determined threshold value were re-examined to ensure the thresholds were representative. For Ki67 positivity, only cells that had a nucleus in the image were considered. Ki67 values were not cell size normalized because the Ki67 signal is exclusive to nuclei.

## Blinded manual artery staging

Arteries were categorized into 5 remodeling stages based on criteria adapted from the 4-stage model proposed by Smith et al[42]. These criteria were previously used to describe spiral arteries observed in H&E and single channel IHC images and were adapted to suit multiplexed MIBI data (Fig. 3a, details in Extended data Fig. S3a). 600 arteries were categorized according to these criteria by a single reviewer using exclusively crops of MIBI pseudocolor overlays (SMA, Vimentin, CD31, H3, and HLA-G) including only the artery (as defined by feature mask) and any EVTs in the lumen. The reviewer was blinded to the rest of the image, serial H&E sections, gestational age, and any clinical data. 12 partially captured arteries were excluded from the final dataset of 588 arteries.

## Automated digitization of artery morphological features

The same format of cropped artery MIBI images that were manually scored by the reviewer were used to calculate a set of geometric parameters for several selected features. These features described the organization and structure of the vessel wall, the continuity of the endothelium and its thickness, and the presence and structure of

intravascular EVTs. In order to capture these features, a structure of concentric circles we termed the "onion" structure is defined, with the outer circle of this structure enclosing the artery and the inner circles dividing it into layers. This structure is described below using the two-dimensional cylindrical coordinate system with the radial axis r, azimuthal (angular) axis ø, and origin of the axis at point (x,y). Point (x,y) is the user defined artery center. For an artery in the binary mask M, the following algorithm was used to create the "onion" structure (Extended Data Fig. S3c):

- Define a circle enclosing the artery, centered at point (x,y) with radius a as follows:
  - (x,y) was taken as the user-defined artery center point
  - a, the radius is defined as the maximum distance between (x,y) and the edge of M – rounded up to the nearest integer multiple of n, such that a=I*n for an integer I. n is a user defined thickness parameter for the "onion" layers.
- Define the inner circles comprising the "onion" layers:
  - Divide the radius a of the outer circle into I equal sections of length n, creating layers along the radial r axis.
  - The radii of the inner circles are then defined as: 0,1*n,2*n,…(I-1)*n.
- Divide the "onion" into k equal sectors along the ø axis, k is a user defined integer.
- Subdivide each sector into segments:
  - The sectors are internally divided by the circles, creating parts with 4 corners and 4 sides, with the 2 sides being straight (sector dividers), and the 2 sides being arcs (parts of ellipse circumferences).
  - The arcs are replaced with secants (straight line connecting the ends of the arc), turning the segment into a trapezoid.
  - The parameters n=10 pixels and k=100 were used to allow for segments large enough to contain a sufficient number of pixels to average expression over.

The following features are then extracted for each artery "onion":

1. Geometrical features:
   a. radius - the maximum distance between any pixel within the mask and the

737 closest pixel on the edge of the mask.
738 b. perimeter – the Euclidean distance between all adjacent pixels on the edge
739 of the artery mask
740 c. area – the total number of pixels within the artery mask
741 2. Protein morphology features, for each of the following markers: CD31, CK7, H3,
742 HLA-G, SMA, VIM
743 a. Average signal – weighted-average over segments of marker expression,
744 where the weight of a segment corresponds to the number of pixels it
745 contains. Weighted average was used to avoid smaller inner segments
746 having disproportionate effect on the average.
747 b. Thickness –
748 i. For each sector we calculate the distance d between the inner-most
749 segment positive for the marker and the outer-most positive
750 segment. Positivity is measured by comparing the mean signal over
751 pixels the segment to a user defined threshold.
752 ii. The mean and standard deviation of thickness are calculated as the
753 mean and standard deviation of d over all sectors.
754 c. Radial coverage - the percentage of sectors positive for marker signal. A
755 sector is considered positive if the mean signal over sector pixels accedes
756 a user defined threshold.
757 d. Jaggedness – This feature measures the extent jaggedness of an artery
758 outline. To do so, first a skeletonization function written by Nicholas R.
759 Howe [62] is applied to the artery mask, this function returns a “skeleton” of
760 the artery outline. This “skeleton” also assigns values to the outline pixels
761 based on their distance from the core shape. Then, two different
762 binarization thresholds are chosen: a “non- branch” threshold (a high value
763 = 60 pixels, indicating greater topological distance and a “branch” threshold
764 (a low value = 5 pixels, indicating smaller topological distance). The ratio
765 between the total number of “non branch” and “branch” pixels is the
766 jaggedness.

## Calculation of continuous SAR remodeling score δ

A supervised dimensionality reduction technique based on linear discriminant analysis (LDA)[43] (code URL: https://github.com/davidrglass) was employed using the per artery digitized morphological features and manually assigned remodeling stage labels as inputs. All artery morphology feature values were standardized (mean subtracted and divided by the standard deviation) and all arteries were used as training data. The LDA output was:

a. The optimal linear combination of a subset of features, that maximized the separation by manual stage between arteries in LDA space (Supplementary Table 6)
b. The coordinates of each artery in LDA space (Supplementary Table 5)

In order to define the SAR trajectory, a fourth-degree polynomial was fitted to the artery coordinates in LDA space. To determine the optimal degree of the polynomial, polynomials with degrees 1-6 were fitted and the degree that minimized the p-value for separating δ distributions between arteries grouped by manual remodeling stage (Extended Data Fig. S3f) was selected. The polynomial fit was implemented using the MATLAB function fit and resulted in the following polynomial: $f(x) = 0.0005*x^4 - 0.01227*x^3 + 0.1363*x^2 - 0.4354*x - 0.7425$. The polynomial was then numerically interpolated on a dense $10^4$ point grid and the distance from each artery point in LDA space to the polynomial was calculated using this grid and the MATLAB exchange function distance2curve [63]. δ per artery was then calculated as the line integral from the curve origin to closest point to the artery on the curve (Fig. 3n, inset). This integral was numerically calculated using a custom MATLAB script. δ values were linearly rescaled to the range 1-5 using the MATLAB function rescale.

## Cell type frequency as function of GA and SAR

For examining cell type frequencies within the decidua as function of GA and SAR (Fig. 3, Fig. 4), per image cell frequency tables were constructed in which cell type frequencies were calculated as the proportion of cells in the decidua feature mask of that image. Cells located in other feature masks (artery, gland, vessel, or cell column masks) were not counted, nor were cells of an unassigned type (‘other’). In order to focus these

797 analyses on cell populations strictly found in the decidua, muscle and glandular cells were
798 also excluded; these cell types occasionally extended outside of their artery and gland
799 feature masks, respectively. Cell frequency as a function of GA for a cell type was defined
800 as the per image proportion values for that cell type, as function of the GAs associated
801 with the images. Similarly, cell frequency as a function of SAR for a cell type was defined
802 as the per image proportions of that cell type, as function of the mean δ values per image.
803 For the volcano plot in Fig. 3o, we fitted a linear regression model to the two above-
804 described functions. All linear regression models were implemented using the MATLAB
805 function fitlm and the volcano plot only shows points for which regression $R^2 \geq 0.05$. $R^2$
806 and p-values for all δ and GA based regressions can be found in Supplementary Table
807 7. The ration between $R^2$ in the two regression models was used to classify trends as GA-
808 driven, SAR-driven or synchronized. For example, the increase in EVTs out of all cells,
809 R_EVT, was classified as GA-driven because $R^2$ for R_EVT as a function of δ was 0.3,
810 but only 0.1 for R_EVT as a function of GA (Extended Data Figure S3g, Supplementary
811 Table 7). Another example is the increase in macrophages out of immune cells,
812 I_sumMac: it was classified as GA-driven since $R^2$ for I_sumMac as a function of GA was
813 0.6 but only 0.1 for I_sumMac as a function of δ (Extended Data Figure S3f,
814 Supplementary Table 7). For determining trend sizes depicted in Fig. 3o, the following
815 calculation was used: denote the per image frequencies of a cell type as V, and the
816 corresponding per image temporal stamps (either GA or mean image δ) as X. Trend size
817 is then calculated as the difference between the first and last time point in units of the
818 mean: $\frac{V(\max(X))-V(\min(X))}{mean(V)}$.

819 ## Functional markers positivity rate per cell type as function of GA and SAR

820 For examining cell type specific temporal trends in the expression of functional
821 markers (Fig. 5a), 48 combinations of cell type- functional marker were selected. The
822 selected combinations were those for which the positivity frequency Z-score exceeded
823 0.5 (Fig. 2a, right panel). For each of these combinations, the frequency of cells positive
824 for the functional marker was calculated as the number of cells positive for the marker
825 (see “Definition of thresholds for functional marker positivity”), out of the total number of
826 cells of the same cell type in the image. All cells except those located within the cell

column mask were included to focus the analysis on functional marker trends of maternal cells and EVTs that had infiltrated the decidua. For glandular cells, the location was further restricted to the glands mask. The frequency of cells positive for a functional marker as a function of GA, for a cell type, was defined as the per image positivity proportion values as function of the GAs associated with the images. Similarly, marker positivity frequency as a function of SAR for a cell type was defined as the per image proportions of that cell type positive for the marker, as function of the mean δ values per image. For the volcano plot in Fig. 5a, we fitted a linear regression model to the two above-described functions. All linear regression models were implemented using the MATLAB function fitlm and the volcano plot only shows points for which regression $R^2 \geq 0.05$. $R^2$ and p-values for all δ and GA based regressions can be found in Supplementary Table 8. For determining trend sizes depicted in Fig. 5a, the following calculation was used: denote the linear fit to the per-image marker positivity proportion of a cell type as V, and the corresponding per image temporal stamps (either GA or mean image δ) as X. Trend size is then calculated as the difference between the first and last time point in units of the mean: $\frac{V(\max(X))-V(\min(X))}{mean(V)}$.

## Ridge regression for predicting GA from immune composition

Ridge regression was implemented using the sklearn Python package (sklearn.linear_model.Ridge, RidgeCV). Per-image immune frequencies were rescaled to the range 0-1 prior to model fitting, using the sklearn scaling function. Images with fewer than 10 immune cells were excluded (n=8). A randomly derived test-train split of 30/70 was used and GA distribution was verified to be equally represented in the test and train sets (Extended Data Fig. S4a). Ridge regression adds a regularization penalty to the loss function in order to prevent over or under representation of correlated variables, such as immune cell populations. The penalty used for the test set (0.81) was selected using Leave-One-Out Cross-Validation on the training set.

## Definition of anatomical EVT location and associated arteries

Cell column EVTs were defined as EVTs located within cell column masks, intravascular EVTs were located within artery masks, and interstitial EVTs were located

in the decidua. Perivascular EVTs were defined as interstitial EVTs located within 50 pixels of the edge of an artery, as defined by radial expansion of the artery masks (Fig. 6b). Arteries were said to have perivascular or intravascular EVT (Figs. 6f-h) if the number of EVT in the appropriate artery compartment was $\geq$5. For Fig. 6j, only images that contained all four EVT types were considered and cell to artery distance was measured from the cell centroid as detected by segmentation to the border of the artery mask. For Fig. 6i, one image was excluded (16_31762_20_8) due to abnormal tissue morphology.

## SMA and endothelium loss scores

The loss scores presented in Fig. 6g, h were based on digitized morphological features. For SMA, the average feature was used and for endothelium, the radial coverage of CD31 (see “Automated digitization of artery morphological features”). The values for each of the two features were then divided by their maximum across arteries and subtracted from 1 to obtain a loss score. The resulting values were then linearly rescaled to the range 0-1 using the MATLAB function rescale.

## LDA of EVTs by compartment

A method similar to our calculation of the continuous SAR remodeling score δ was used for compartment-wise analysis of EVT types. The input table consisted of marker expression values per EVT. Lineage and functional markers expressed by EVTs were included: CD56, CD57, HLA-G, CK7, PD-L1 and Ki67 (Fig. 2a). EVTs were labeled by spatial compartment: cell column, interstitial, perivascular or intravascular (see “Definition of anatomical EVT location”). Marker expression values were standardized (mean subtracted and divided by the standard deviation) and cell column, interstitial, and intravascular location labels per EVT were used for training the LDA model. Perivascular EVTs were withheld as a test set. Due to the small number or features (markers) a one-dimensional LDA was calculated yielding a single coordinate LD1. LD1 was the optimal linear combination of a subset of markers, to maximize the separation by compartment between EVTs (Supplementary Table 10). LD1 values were subsequently calculated for the withheld test set of perivascular EVTs (Supplementary Table 11). To calculate the difference in similarity to intravascular EVT between interstitial and perivascular, the following calculation was used: intravascular-perivascular similarity was defined as

$sim_{intra-peri} = mean(Ld1_{intravascular}) - mean(Ld1_{perivascular})$. Similarly, intravascular-interstitial similarity was defined as $sim_{intra-inter} = mean(Ld1_{intravascular}) - mean(Ld1_{interstitial})$. The difference in these similarities was then calculated as: $\frac{sim_{intra-inter} - sim_{intra-peri}}{im_{intra-inter}}$ in %.

## Statistical analyses

Throughout the paper, the Kruskal-Wallis test was implemented using the MATLAB function KruskalWallis. All linear regression models were implemented using the MATLAB function fitlm unless stated otherwise. The sided Wilcoxon signed rank test for paired analysis in Extended Data Fig. S6 was implemented using the MATLAB function signrank. MATLAB version used throughout the paper for statistical analysis is MATLAB 2020b.

## Data availability

Imaging data, segmentation masks, and extracted features will be made publicly available prior to publication. Code is currently available upon request and will be made public prior to publication.

# References

1. Moffett-King, A. Natural killer cells and pregnancy. *Nature reviews. Immunology* **2**, 656–663 (2002).

2. Red-Horse, K. *et al.* Trophoblast differentiation during embryo implantation and formation of the maternal-fetal interface. *The Journal of clinical investigation* **114**, 744–754 (2004).

3. Menkhorst, E., Winship, A., van Sinderen, M. & Dimitriadis, E. Human extravillous trophoblast invasion: intrinsic and extrinsic regulation. *Reproduction, fertility, and development* **28**, 406–415 (2016).

4. Vento-Tormo, R. *et al.* Single-cell reconstruction of the early maternal–fetal interface in humans. *Nature* **563**, 347–353 (2018).

5. Suryawanshi, H. *et al.* A single-cell survey of the human first-trimester placenta and

decidua. *Science Advances* **4**, eaau4788 (2018).

6. Mor, G., Aldo, P. & Alvero, A. The unique immunological and microbial aspects of pregnancy. *Nature reviews. Immunology* **17**, 469–482 (2017).

7. Kam, E. P. Y., Gardner, L., Loke, Y. W. & King, A. The role of trophoblast in the physiological change in decidual spiral arteries. *Human Reproduction* **14**, (1999).

8. Whitley, G. S. J. & Cartwright, J. E. Cellular and Molecular Regulation of Spiral Artery Remodelling: Lessons from the Cardiovascular Field. *Placenta* **31**, 465–474 (2010).

9. Pijnenborg, R., Vercruysse, L. & Hanssens, M. The Uterine Spiral Arteries In Human Pregnancy: Facts and Controversies. *Placenta* vol. 27 939–958 (2006).

10. Kliman, H. J. Uteroplacental Blood Flow: The Story of Decidualization, Menstruation, and Trophoblast Invasion. *The American Journal of Pathology* **157**, 1759–1768 (2000).

11. Burton, G. J., Woods, A. W., Jauniaux, E. & Kingdom, J. C. P. Rheological and Physiological Consequences of Conversion of the Maternal Spiral Arteries for Uteroplacental Blood Flow during Human Pregnancy. *Placenta* **30**, 473–482 (2009).

12. Khong, T., de Wolf, F., Robertson, W. & Brosens, I. Inadequate maternal vascular response to placentation in pregnancies complicated by pre-eclampsia and by small-for-gestational age infants. *British journal of obstetrics and gynaecology* **93**, 1049–1059 (1986).

13. Brosens, I., Pijnenborg, R., Vercruysse, L. & Romero, R. THE “GREAT OBSTETRICAL SYNDROMES” ARE ASSOCIATED WITH DISORDERS OF DEEP PLACENTATION. *American Journal of Obstetrics and Gynecology* **204**, 193 (2011).

14. Carter, A. M. Animal Models of Human Placentation – A Review. *Placenta* **28**, S41–S47 (2007).

15. Schmidt, A., Morales-Prieto, D. M., Pastuschek, J., Fröhlich, K. & Markert, U. R.

941 Only humans have human placentas: molecular differences between mice and
942 humans. *Journal of Reproductive Immunology* **108**, 65–71 (2015).

943 16. Pijnenborg, R., Vercruysse, L. & Carter, A. M. Deep trophoblast invasion and spiral
944 artery remodelling in the placental bed of the lowland gorilla. *Placenta* **32**, 586–591
945 (2011).

946 17. Pijnenborg, R., Vercruysse, L. & Carter, A. M. Deep trophoblast invasion and spiral
947 artery remodelling in the placental bed of the chimpanzee. *Placenta* **32**, 400–408
948 (2011).

949 18. Gaynor, L. M. & Colucci, F. Uterine Natural Killer Cells: Functional Distinctions and
950 Influence on Pregnancy in Humans and Mice. *Frontiers in Immunology* **0**, 467
951 (2017).

952 19. Yang, F., Zheng, Q. & Jin, L. Dynamic Function and Composition Changes of
953 Immune Cells During Normal and Pathological Pregnancy at the Maternal-Fetal
954 Interface. *Frontiers in Immunology* **10**, 2317 (2019).

955 20. Pijnenborg, R., Bland, J. M., Robertson, W. B. & Brosens, I. Uteroplacental arterial
956 changes related to interstitial trophoblast migration in early human pregnancy.
957 *Placenta* **4**, 397–413 (1983).

958 21. Chaline, J. Increased cranial capacity in hominid evolution and preeclampsia.
959 *Journal of reproductive immunology* **59**, 137–152 (2003).

960 22. Rockwell, C., Vargas, E. & Moore, L. G. Human physiological adaptation to
961 pregnancy: Inter- and intraspecific perspectives. *American Journal of Human*
962 *Biology* **15**, 330–341 (2003).

963 23. Zhu, H., Hou, C. C., Luo, L. F., Hu, Y. J. & Yang, W. X. Endometrial stromal cells
964 and decidualized stromal cells: Origins, transformation and functions. *Gene* **551**,
965 1–14 (2014).

966 24. TANG, B., GULLER, S. & GURPIDE, E. Mechanism of Human Endometrial Stromal
967 Cells Decidualization. *Annals of the New York Academy of Sciences* **734**, 19–25
968 (1994).

969 25. Moffett, A. & Colucci, F. Uterine NK cells: active regulators at the maternal-fetal
970 interface. *The Journal of clinical investigation* **124**, 1872–1879 (2014).

971 26. Robson, A. *et al.* Uterine natural killer cells initiate spiral artery remodeling in human
972 pregnancy. *The FASEB Journal* **26**, 4876–4885 (2012).

973 27. Craven, C. M., Morgan, T. & Ward, K. Decidual spiral artery remodelling begins
974 before cellular interaction with cytotrophoblasts. *Placenta* **19**, 241–252 (1998).

975 28. Keren, L. *et al.* MIBI-TOF: A multiplexed imaging platform relates cellular
976 phenotypes and tissue structure. *Science Advances* **5**, eaax5851 (2019).

977 29. Chang, R.-Q., Li, D.-J. & Li, M.-Q. The role of indoleamine-2,3-dioxygenase in
978 normal and pathological pregnancies. *American Journal of Reproductive*
979 *Immunology* **79**, e12786 (2018).

980 30. Yasinska, I. M. *et al.* The Tim-3-Galectin-9 Pathway and Its Regulatory
981 Mechanisms in Human Breast Cancer. *Frontiers in Immunology* **0**, 1594 (2019).

982 31. Li, M. *et al.* Tim-3/CTLA-4 pathways regulate decidual immune cells-extravillous
983 trophoblasts interaction by IL-4 and IL-10. *FASEB journal : official publication of the*
984 *Federation of American Societies for Experimental Biology* **35**, (2021).

985 32. Hu, X. *et al.* Newly characterized decidual Tim-3+ Treg cells are abundant during
986 early pregnancy and driven by IL-27 coordinately with Gal-9 from trophoblasts.
987 *Human reproduction (Oxford, England)* **35**, 2454–2466 (2020).

988 33. Wang, S. *et al.* Tim-3 protects decidual stromal cells from toll-like receptor-
989 mediated apoptosis and inflammatory reactions and promotes Th2 bias at the
990 maternal-fetal interface. *Scientific Reports 2015 5:1* **5**, 1–9 (2015).

991 34. Sedlmayr, P. *et al.* Localization of indoleamine 2,3-dioxygenase in human female
992 reproductive organs and the placenta. *Molecular Human Reproduction* **8**, 385–391
993 (2002).

994 35. Baranski, A. *et al.* MAUI (MBI Analysis User Interface)-An image processing
995 pipeline for Multiplexed Mass Based Imaging. *PLoS computational biology* **17**,
996 (2021).

997 36. Greenwald, N. F. *et al.* Whole-cell segmentation of tissue images with human-level
998 performance using large-scale data annotation and deep learning. *bioRxiv*
999 2021.03.01.431313 (2021) doi:10.1101/2021.03.01.431313.

1000 37. van Gassen, S. *et al.* FlowSOM: Using self-organizing maps for visualization and
1001 interpretation of cytometry data. *Cytometry Part A* **87**, 636–645 (2015).

1002 38. Faas, M. M. & de Vos, P. Uterine NK cells and macrophages in pregnancy. *Placenta*
1003 **56**, 44–52 (2017).

1004 39. Kämmerer, U. *et al.* Unique Appearance of Proliferating Antigen-Presenting Cells
1005 Expressing DC-SIGN (CD209) in the Decidua of Early Human Pregnancy. *The*
1006 *American Journal of Pathology* **162**, 887–896 (2003).

1007 40. Huhn, O. *et al.* Distinctive phenotypes and functions of innate lymphoid cells in
1008 human decidua during early pregnancy. *Nature Communications* **11**, (2020).

1009 41. Salvany-Celades, M. *et al.* Three Types of Functional Regulatory T Cells Control T
1010 Cell Responses at the Human Maternal-Fetal Interface. *Cell Reports* **27**, 2537-
1011 2547.e5 (2019).

1012 42. Smith, S. D., Dunk, C. E., Aplin, J. D., Harris, L. K. & Jones, R. L. Evidence for
1013 immune cell involvement in decidual spiral arteriole remodeling in early human
1014 pregnancy. *American Journal of Pathology* **174**, 1959–1971 (2009).

1015 43. Tsai, A. G. *et al.* Multiplexed single-cell morphometry for hematopathology
1016 diagnostics. *Nature Medicine* **26**, (2020).

1017 44. Nielsen, C. M., White, M. J., Goodier, M. R. & Riley, E. M. Functional significance
1018 of CD57 expression on human NK cells and relevance to disease. *Frontiers in*
1019 *Immunology* vol. 4 (2013).

1020 45. Gonçalves Silva, I. *et al.* The Tim-3-galectin-9 Secretory Pathway is Involved in the
1021 Immune Escape of Human Acute Myeloid Leukemia Cells. *EBioMedicine* **22**, 44–
1022 57 (2017).

1023 46. Blois, S. M. *et al.* Role of galectin-glycan circuits in reproduction: from healthy
1024 pregnancy to preterm birth (PTB). *Seminars in Immunopathology 2020 42:4* **42**,

469–486 (2020).

47. Blois, S. M. *et al.* Pregnancy Galectinology: Insights Into a Complex Network of Glycan Binding Proteins. *Frontiers in Immunology* **0**, 1166 (2019).

48. Robillard, P. Y., Dekker, G. A. & Hulsey, T. C. Evolutionary adaptations to pre-eclampsia/eclampsia in humans: Low fecundability rate, loss of oestrus, prohibitions of incest and systematic polyandry. *American Journal of Reproductive Immunology* vol. 47 104–111 (2002).

49. Naruse, K. *et al.* Localization of matrix metalloproteinase (MMP)-2, MMP-9 and tissue inhibitors for MMPs (TIMPs) in uterine natural killer cells in early human pregnancy. *Human Reproduction* **24**, 553–561 (2009).

50. Hunt, J., Petroff, M., McIntire, R. & Ober, C. HLA-G and immune tolerance in pregnancy. *FASEB journal : official publication of the Federation of American Societies for Experimental Biology* **19**, 681–693 (2005).

51. Tilburgs, T., Evans JH, Crespo, Â. & Strominger, J. The HLA-G cycle provides for both NK tolerance and immunity at the maternal-fetal interface. *Proceedings of the National Academy of Sciences of the United States of America* **112**, 13312–13317 (2015).

52. Isaka, K. *et al.* Expression and Activity of Matrix Metalloproteinase 2 and 9 in Human Trophoblasts. *Placenta* **24**, 53–64 (2003).

53. Harris, L. K., Jones, C. J. P. & Aplin, J. D. Adhesion Molecules in Human Trophoblast – A Review. II. Extravillous Trophoblast. *Placenta* **30**, 299–304 (2009).

54. None, K. *et al.* Evolution of placental invasion and cancer metastasis are causally linked. *Nature ecology & evolution* **3**, 1743–1753 (2019).

55. Bulmer, J., Thrower, S. & Wells, M. Expression of epidermal growth factor receptor and transferrin receptor by human trophoblast populations. *American journal of reproductive immunology (New York, N.Y. : 1989)* **21**, 87–93 (1989).

56. Wright JK *et al.* HER1 signaling mediates extravillous trophoblast differentiation in humans. *Biology of reproduction* **83**, 1036–1045 (2010).

57. Coorens, T. H. H. *et al.* Inherent mosaicism and extensive mutation of human placentas. *Nature 2021 592:7852* **592**, 80–85 (2021).

58. Angelo, M. *et al.* Multiplexed ion beam imaging of human breast tumors. *Nature Medicine* **20**, 436–442 (2014).

59. McCaffrey, E. F. *et al.* Multiplexed imaging of human tuberculosis granulomas uncovers immunoregulatory features conserved across tissue and blood. *bioRxiv* 2020.06.08.140426 (2020) doi:10.1101/2020.06.08.140426.

60. Risom, T. *et al.* Transition to invasive breast cancer is associated with progressive changes in the structure and composition of tumor stroma. *bioRxiv* 2021.01.05.425362 (2021) doi:10.1101/2021.01.05.425362.

61. Keren, L. *et al.* A Structured Tumor-Immune Microenvironment in Triple Negative Breast Cancer Revealed by Multiplexed Ion Beam Imaging. *Cell* **174**, 1373-1387.e19 (2018).

62. Howe, N. Better Skeletonization - File Exchange - MATLAB Central. https://www.mathworks.com/matlabcentral/fileexchange/11123-better-skeletonization.

63. D'Errico, J. distance2curve - File Exchange - MATLAB Central. https://www.mathworks.com/matlabcentral/fileexchange/34869-distance2curve.

## Acknowledgements

We thank V. Winn, N. Vivanco, A. Moore, E. McCaffrey, D. Glass, T. Risom, J. P. Oliveria, K. O'Neill and C. Coutifaris for comments. M.A. is supported by 5U54CA20997105, 5DP5OD01982205, 1R01CA24063801A1, 5R01AG06827902, 5UH3CA24663303, 5R01CA22952904, 1U24CA22430901, 5R01AG05791504, and 5R01AG05628705 from NIH, W81XWH2110143 from DOD, and other funding from the Bill and Malinda Gates Foundation, Cancer Research Institute, the Parker Center for Cancer Immunotherapy, and the Breast Cancer Research Foundation. S.G is supported by the Bill and Melinda Gates Foundation OPP1113682. I.A. is an awardee of the

Weizmann Institute of Science – Israel National Postdoctoral Award Program for Advancing Women in Science. E.S is supported by National Science Scholarship, Agency for Science, Technology, and Research (A*STAR), Singapore.

## Author contributions

S.G. assembled the tissue cohort, performed and designed experiments, annotated images, analyzed and interpreted data and wrote the manuscript. I.A. analyzed and interpreted data, wrote the manuscript. E.S. performed and designed experiments, annotated images, analyzed and interpreted data, wrote the manuscript. G.R. advised on cohort design, assembled tissue cohort, annotated images. A.B, N.G., G.M., M.S., W.G. and D.V.V. wrote software for image analysis. M.B. advised on experimental design and reagent validation. E.J. assembled cohort patient metadata. L.K. advised on computational analysis. Z.K. Prepared and validated reagents. S.K. Constructed the tissue microarray. S.W. annotated images. T.H. validated reagents and advised on experimental design. M.R. oversaw tissue microarray construction. M.A. conceived the study, advised on experimental design and data analysis, wrote the manuscript.

## Supplementary table legends

**Supplementary Table 1 - Patients table.** This table provides patient meta-data such as age, ethnicity, body mass index, parity and relevant medical conditions such as HIV.

**Supplementary Table 2 - Information on the histological characteristics of the blocks retrieved, including the presence of cell column anchoring villi.** This table shows, for each patient's block, whether cell column anchoring villi were present (1) or absent (0), and the number of regions containing spiral arteries annotated as appropriate for TMA construction by the pathologist (Methods). In blocks containing ≥ 2 distinct, separate pieces of tissue, cell column villi were considered present if they were present on any piece containing pathologist annotations.

**Supplementary Table 3 - Cell table.** This table enumerates all single cells in this study and provides their location, morphological characteristics such as size and shape,

marker expression, FlowSOM cluster assignment and cell type assignment.

**Supplementary Table 4 - Positivity binary threshold for functional markers.** This table provides binary expression thresholds per functional marker- used to determine whether cells are positive for that marker (See methods).

**Supplementary Table 5 - Artery properties and staging.** This table provides arteries meta-data, including their measured digitized morphological features (see Methods), manual stage and remodeling score δ.

**Supplementary Table 6 - LDA coefficients for artery morphological features.** This table contains the coefficients per artery feature that define the LDA space used for digitized artery staging (Fig. 3n). For the features selected by the algorithm, their ld1 and ld2 coefficients are listed. Additional columns show the Z scored absolute values of these coefficients.

**Supplementary Table 7 - Regression results for cell type proportions as a function of GA and δ.** This table provides the values plotted in Fig. 3o. Each row represents a cell proportion with those starting with R_ indication proportion out of all cells in the image, I_ - proportion out of immune cells in image, N_- proportion out of NK cells in image, M_ proportion out of macrophages in image, T_- proportion out of T cells in image, F_- proportion out of EVT in image, S_ proportion out of structural cells in image (Fig. 2b). The columns show values for the linear regression on per image proportions as function of GA and remodeling score δ: the log transformed ratio of $R^2$, the maximal obtained regression $R^2$ (maximal between GA and δ), the minimal obtained regression p-value and trend size (see Methods).

**Supplementary Table 8 - Regression results for functional markers expression as a function of GA and δ.** This table provides the values plotted in Fig. 5a. Each row represents a combination of a cell type and a functional marker. The columns show values for the linear regression on per image marker positivity rates for the marker-cell type as function of GA and remodeling score δ: the log transformed ratio of $R^2$, the maximal obtained regression $R^2$ (maximal between GA and δ), the minimal obtained regression p-value and trend size (see Methods).

**Supplementary Table 9 - Information on antibodies, metal reporters, staining concentrations, and parameters used for low-level processing of MIBI data.** This table contains, for each marker, relevant antibody information including clone, vendor, vendor ID, channel and elemental reporter, and final staining titers used. The parameters used for marker-specific low-level processing of MIBI data (background removal, denoising, and aggregate removal steps as previously described) are also shown.

**Supplementary Table 10 - LD1 coefficients for markers expressed by EVT.** This table contains the coefficients per EVT expressed marker that define the LDA space used for measuring similarity between anatomical tissue compartments (see Methods, Extended Data Fig. 6c). For the markers selected by the algorithm, their ld1 coefficients are listed. An additional column shows the Z scored absolute values of these coefficients.

**Supplementary Table 11 - LD1 values per EVT.** This table shows ld1 values per single EVT with LDA input- standardized marker expression values (see Methods, Extended Data Fig. 6c). Additional metadata such as EVT type, anatomical location, the image the cell was taken from is also provided.